The assessment of the Geogenic Radon Potential of the Euganean Hills volcanic district (Italy) by using spatial regression kriging.

Chiara Coletti[1], Giancarlo Ciotoli[2], Eleonora Benà[1], Erika Brattich[3], Giorgia Cinelli[4], Antonio Galgaro[1], Matteo Massironi[1], Claudio Mazzoli[1], Domiziano Mostacci[5], Paolo Mozzi[1], Jacopo Nava[1], Livio Ruggiero[6], Alessandra Sciarra[4], Laura Tositti[7], Raffaele Sassi[1]

[1] Department of Geosciences, University of Padova, Via Gradenigo 6, 25131 Padova, Italy

[2] Institute of Environmental Geology and Geoengineering, National Research Council, 00015 Rome, Italy

[3] Department of Physics and Astronomy, University of Bologna, via Irnerio 46, 40126 Bologna, Italy

[4] European Commission, Joint Research Centre (JRC), Via Enrico Fermi 2749, 21027 Ispra VA, Italy

[5] Department of Industrial Engineering, University of Bologna, Via dei Colli 16, 40136 Bologna, Italy

[6] National Institute of Geophysics and Volcanology, Via Vigna Murata 605, 00143 Rome, Italy

[7] Department of Chemistry "G. Ciamician", University of Bologna, Via Selmi 2, 40126 Bologna, Italy

Abstract (300 words)

The assessment of potential radon hazardous environments due to the terrestrial ionizing radiation sources is nowadays a critical issue in planning, monitoring, and developing appropriate mitigation strategies. Although some geological structures (e.g., faults) and other geological factors (e.g., radionuclide content, soil organic or rock weathering) can locally affect the radon occurrence, at the basis of a good implementation of radon-safe systems, optimized modelling at territorial scale is required. The use of spatial regression models, adequately combining different types of predictors, represents an invaluable tool to identify the relationships between radon and its controlling factors and to construct Geogenic Radon Potential (GRP) map of an area. In this work, two GRP maps were developed based on field measurements of soil gas radon and thoron concentrations and radionuclide measurements of soil and rock samples carried out in Euganean Hills (northern Italy) area. A predictive model of radon concentrations in soil gas was reconstructed taking into account the

relationships among the soil gas radon and seven predictors: total gamma dose radiation (TGDR), thoron (^{220}Rn), fault density (FD), soil permeability (PERM), digital terrain model (SLOPE), moisture index (TMI), heat load index (HLI). These predictors were chosen to elaborate local spatial models by using the Empirical Bayesian Regression Kriging (EBRK) in order to find the best combination and define the GRP of the Euganean Hill area. A second GRP map based on the Neznal approach (called GRP_{NEZ}) has been modelled using the TGDR and ^{220}Rn, as predictors of radon concentration, and FD as predictor of the soil permeability. Then, the two GRP maps have been compared. Results highlight that the bedrock type mainly contributes to the radon potential but integrated with the presence of faults and topographic features that affect radon migration in the subsoil and its exhalation at the soil/atmosphere boundary.

Graphical abstract

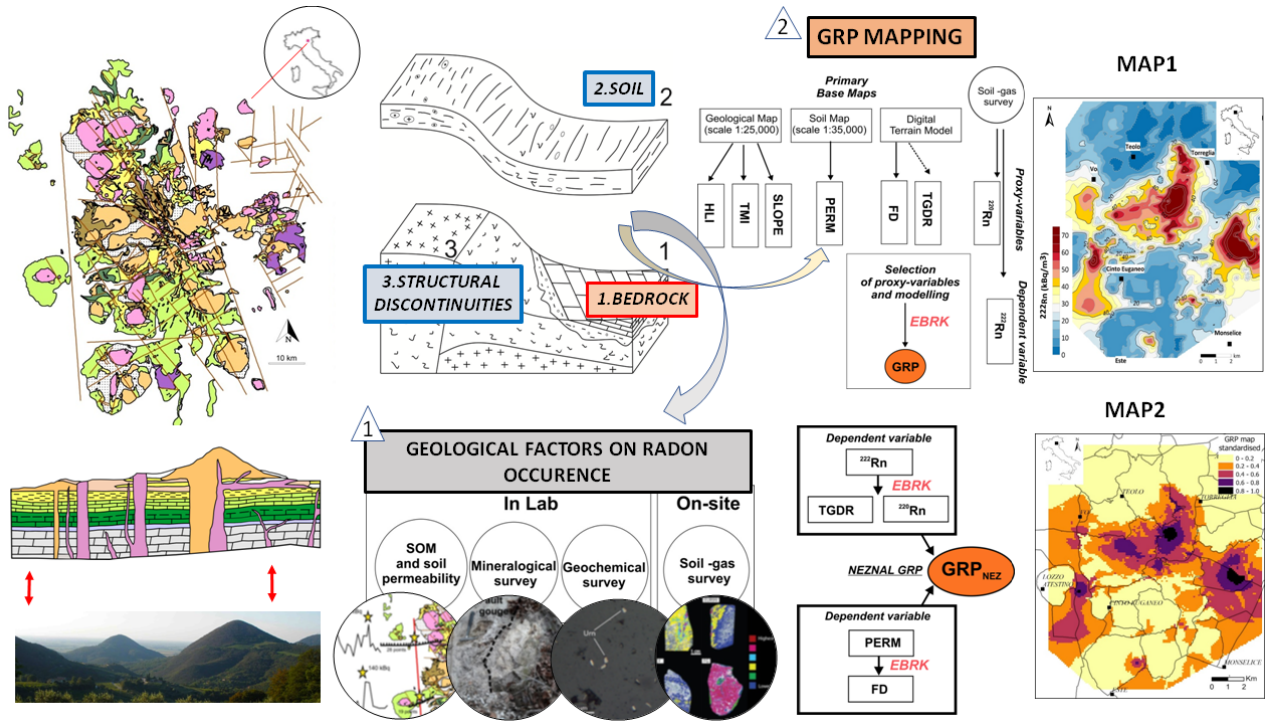

Highlights (3-5; 85 characters):

- Geological structures and other factors can locally affect radon occurrence.
- The correlation between different proxies represents the best way for assessing the radon risk.

- The EBRK is a useful tool to construct a GRP map.
- The Neznal formula by using regression kriging maps is a reliable approach to obtain a GRP map.
- A deep knowledge on the terrestrial contribution develops appropriate territorial strategies.

Keywords: Natural radioactivity; radon; Geogenic Radon Potential; Regression Kriging; Geostatistics.

1. Introduction

WHO (World Health Organization, 2009) has long recognised indoor radon as the second leading cause of lung cancer incidence after cigarette smoking (European Commission, 2021; National Research Council, 1999). Nowadays, scientific community and national authorities are deeply involved in the study and the knowledge of the sources and the controlling factors relevant to radon migration in the subsoil and exhalation at surface to develop efficient safety policies and to improve mitigation systems.

World population is continuously exposed to two main natural ionizing radiations: i) the cosmic contribution, from secondary radiation released by high-energy cosmic rays' incident on the Earth's atmosphere; and ii) the terrestrial contribution, from the residual radioactive nuclides generated during the formation of the Earth and still present in the Earth's crust (UNSCEAR, 2017; Cinelli et al, 2019). Rocks and soils can, indeed, contain hazardous natural radionuclides, as a function of their lithology and subsequent evolution, mainly represented by uranium and thorium radioactive families and the primordial potassium-40. Radon (^{222}Rn), a noble gas, a direct parent nuclide of radium (^{226}Ra) from the ^{238}U series, is the major contributor to the dose received by the global population due to ionizing radiation and it represents a health risk (UNSCEAR, 2008, Annex B).

In order to reliably reconstruct the actual exposure from natural ionising radiation and to find proper solutions, the scientific community implements networks of collaboration among different

70 competences wherein statistics and spatial models, by means of a shared and traceable model
71 approach, and providing reference values and generating harmonized data, i.e. at European level we
72 can mention the Atlas of Natural Radiation (European Commision, 2019) and the MetroRADON
73 project (MetroRADON).
74 Indeed, it is now well-known that radon information solely based on indoor measurements may be
75 seriously biased by unconstrained factors (e.g., type of building materials, floor level, ventilation,
76 presence of a basement, premises function, number of buildings per km^2) leading to a potentially
77 incomplete, if not incorrect, understanding of the risk associated with radon exhalation (European
78 Commision, 2019). A correct approach in this sense requires, in fact, accurate information about the
79 geological and the structural factors that control radon exhalation processes and the inherent potential
80 risk (Ciotoli et al., 2017, 2019). It has been already well established that naturally occurring
81 radionuclides in rock forming minerals and soils may lead to high concentrations of these elements
82 over wide areas in particular geological contexts (Plant et al., 2003; Cuney, 2014). Identifying risk
83 areas requires, therefore, the identification and mapping of the predisposing geological factors and
84 the knowledge on the underground geological environment (Sundal et al., 2004; Appleton, 2006;
85 Yarmoshenko et al., 2016; Ciotoli et al., 2017; Kropat et al. 2017).
86 The Euganean Hills district (100 km^2, northern Italy) represents an ideal case of study because it is a
87 densely populated area characterised by a complex geological context (Fig. 1a), that in the past
88 showed an indoor radon concentration above the national average of 70 Bq/m^3 (Bertolo and Bigliotto?
89 et al. 2009; ANPA, 2000; Bochiccio et al. 1996). In the last decades, some works investigated the
90 possible link between observed indoor radon concentrations and geological and tectonic features of
91 the Euganean area (Trotti et al., 1994, 1998, 1999; Strati et al., 2014). In particular, in 2002 the
92 regional planning of radon monitoring (DGRV n.79, 2002), following the European Recommendation
93 n. 143/90 (European Commission, 1990), measured 189 buildings, 17% of which exceed the reference
94 value of 200 Bq/m^3 indicated in the Recommendation. More recently, the link between the
95 distribution of indoor radon concentration and the lithological characteristics of this area was

preliminarily assessed by ANOVA and geostatistical analysis (Tositti et al., 2017). Results of the latter showed that the U, Th and K content of lithologies explained over 50% of the total variance of the data and identified the areas with high concentrations corresponding to those characterized by volcanic bedrock types, in particular to rhyolites and trachytes.

The present work is aimed to complete the previous investigation (Tositti et al., 2017) by performing on-site soil-gas surveys, extending the analysis of radionuclide content to a higher number of rocks, and considering other important factors which can locally increase the radon occurrence, such as hydrothermal alterations, types of soils (e.g., geochemistry or presence of organic matters), and faults. Moreover, in order to construct a reliable Geogenic Radon Potential map of the Euganean district, an approach based on the Empirical Bayesian Regression Kriging (EBRK) was adopted to study the local spatial relationships by fitting a model between the soil gas radon concentrations (dependent variable) and the following seven predictors (explanatory variables): fault density (FD), total gamma radiation dose (TGDR), thoron ^{220}Rn, digital terrain mode (SLOPE), moisture index (TMI), heat load index (HLI) and soil permeability (PERM)). The spatial model was then adopted to construct a map using the Empirical Bayesian Regression Kriging (EBRK) derived by the selection of the most reliable predictors (TGDR, thoron, FD and Permeability).

In addition, a second GRP map (GRP_{NEZ}) has been elaborated applying the Neznal formula (Neznal et al. 2004) using maps developed by regression kriging: i) the estimated soil gas radon concentration (with radon measured as dependent variables and TGDR and thoron measurements as proxy-variables) and ii) the estimated permeability (where the soil permeability is the dependent variable, and the fault density as proxy-variables).

A comparison between the two GRP maps developed have been reported. Results basically show the GRP_{NEZ} more conservative with regards to anomalous areas, although both approaches are efficient and mostly consistent among them.

The two Geogenic Radon Potential maps can be used as hazard projection tools and represent a useful relatively low-cost step for a preliminary risk assessment to plan new effective radon monitoring

122 survey and prevention strategies in the Euganean Hills district, leading important effects on the
123 territory, in terms of public awareness and action policies.
124
125 **2. The Geogenic Radon Potential (GRP)**
126 The concept of the Geogenic Radon Potential (GRP) has been recently discussed in Bossew et al.
127 2020, where the GRP is the parameter that quantify the amount of radon delivered by the Earth from
128 nearby geological formation to the atmosphere. This quantity can be used as a hazard indicator as it
129 represents the Rn that can potentially be available for the indoor environment, excluding the
130 anthropogenic factors (i.e., building characteristics and living habits) that can also affect Rn indoor
131 levels. The use of GRP is extremely important for its land-use applications in non-developed areas.
132 In the last decades, several approaches were used to define and estimate the GRP of an area (Gruber
133 et al. 2013, Szabó et al. 2014, Bossew 2015, Pásztor et al. 2016; Ciotoli et al., 2017; Giustini et al.,
134 2019; Petermann et al., 2021). However, one of the most used methods to assess the GRP was
135 proposed by Neznal et al. 2004, though it was derived by Kemski et al., 2001. The Neznal formula is
136 reported in the equation 1:
137 $$GRP_{Nez} = \frac{C_{Rn}}{-log_{10}k - 10} \quad (1)$$
138 where GRP_{Nez} is the Geogenic Radon Potential, C_{Rn} is the equilibrium soil gas radon concentration
139 at a definite depth (0.8–1 m) (kBq/m^3) and k is the soil gas permeability (m^2).
140 The GRP can show a spatial and temporal variability as the consequence of the factors which control
141 the radon source (e.g., radionuclide content), migration (e.g., soil/rock permeability, faults) and
142 exhalation (soil moisture and meteorological conditions at the soil/atmosphere boundary).
143 In recent years, the easily available dataset relating to some radon proxy spatial variables (or
144 predictors) coupled with the growing use of Geographic Information System software's and tools and
145 the PCs computing capabilities increased the development of GRP maps by using multivariate
146 techniques (i.e., spatial global and local regressions, such as Ordinary Least Square and
147 Geographically Weighted Regression, Regression Kriging, Machine Learning, etc.) (Ciotoli et al.,

2017; Giustini et al., 2019; Petermann et al., 2021). In this paper, we calculate and compare GRP maps obtained by the application of regression kriging and using Neznal formula with that obtained by the application of regression kriging by using a dataset of different predictors.

3. Study area description

The Euganean Hills district (North-Eastern Italy) covers an area of more than 100 km^2 and forms an isolated volcanic body within the Veneto alluvial plain. The geological landscape of the area is dominated by volcanic formations from Late Eocene to Early Oligocene in age, forming mainly laccoliths and dykes within Late Jurassic to Early Oligocene sedimentary sequences, constituted by limestones and marlstones: the Maiolica Formation (Late Jurassic-Late Cretaceous), the Scaglia Rossa Formation (Late Cretaceous-Early Eocene) and the Torreglia Formation (Early Eocene-Early Oligocene) (Fig. 1b) (; Bartoli et al., 2015). The geological framework of the area is structurally characterized by the interplay between the Tertiary volcano-tectonic structures and regional fault systems associated to the Cenozoic compressional evolution of the northern part of the Adria microplate. In particular, the area is within the complex Lessini-Euganei structural domain which is part of the trascurrent western margin of the Adria Indenter and, at the same time, the western boundary of the foreland of the South Alpine thrust and fold belt (Massironi et al. 2006; Viganò et al, 2015; Viganò et al, 2018). The latter is deformed and translated by a set of NNW transtentional to transpressional faults, whose frequency increases while approaching the Eastern margin of the Euganean Hills, and a series of segmented ENE faults with a prevalent compressional behaviour (Pola et al., 2014, 2015).

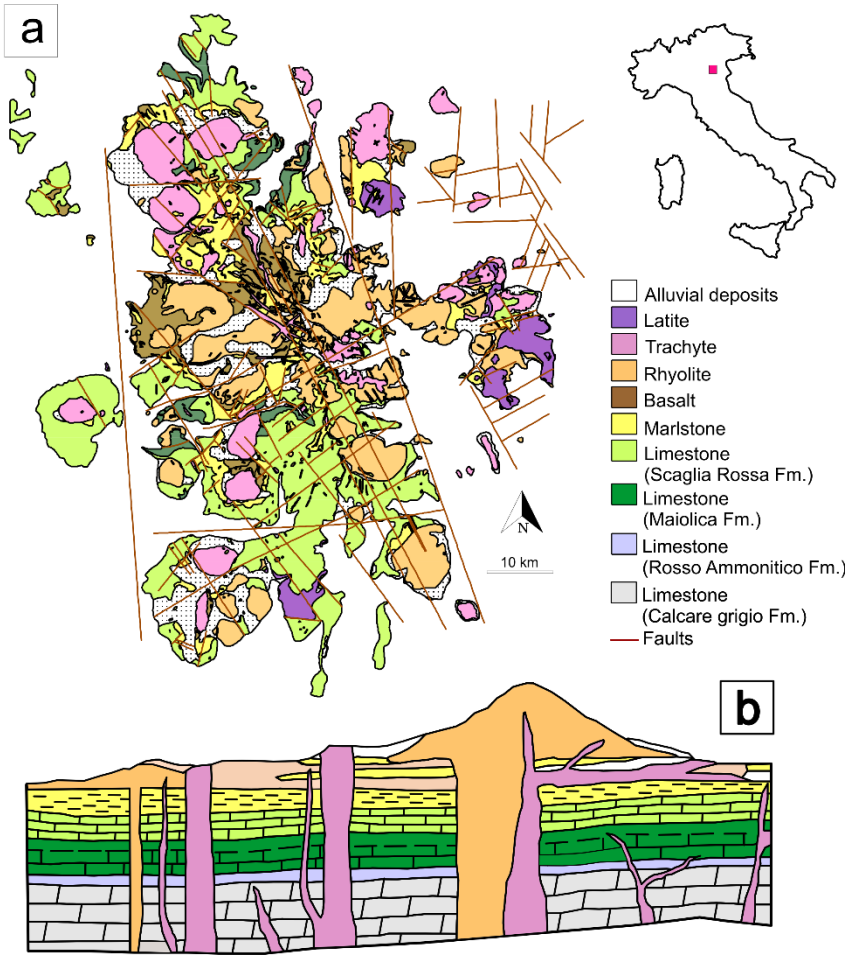

Figure 1: a) Sketch map of the investigated area; b) Scheme of a rhyolite dome on a sedimentary stratigraphy.

4. Materials and methods

4.1 Experimental strategy

In the period 2017-2020, soil-gas surveys were conducted to measure the radon concentration in the soil in the whole studied area to evaluate the radiogenic soil potential (Fig. 1S) and the effect of the fault channelling. In this period, further rock samples (respect to data reported in Tositti et al., 2017, Fig. 1S) were collected for the analysis of the radionuclide content, also including colluvial and alluvial soils to ensure the representativeness of all outcropping lithologies and to understand the connection between lithologies and different factors which regulate the radon migration and exhalation, such as hydrothermal alterations, types of soils (e.g., geochemistry or presence of organic matters), and faults (Fig. 2).

In this work, all collected data was used to define the GRP of the Euganean Hills (northern Italy) area based on field measurements of soil gas radon and thoron concentrations and radionuclide measurements of soil and rock samples. In particular, we constructed a predictive regression model of radon concentrations in soil gas by analysing its relationships with some predictors (see par. 4.6) explained by a GRP map. In addition, a second GRP map has been elaborated applying the Neznal formula (Neznal et al. 2004) by using the Empirical Bayesian Kriging to fit two regression models: i) the source model using TGDR and thoron (^{220}Rn) as predictors of radon concentration using Rn as response variable, and ii) a migration model using FD as a function of the soil permeability as response variable. Data were elaborated by using geostatistical techniques in order to provide a reliable GRP of the area (see par. 4.6).

Figure 2 shows the flowchart of the applied procedures.

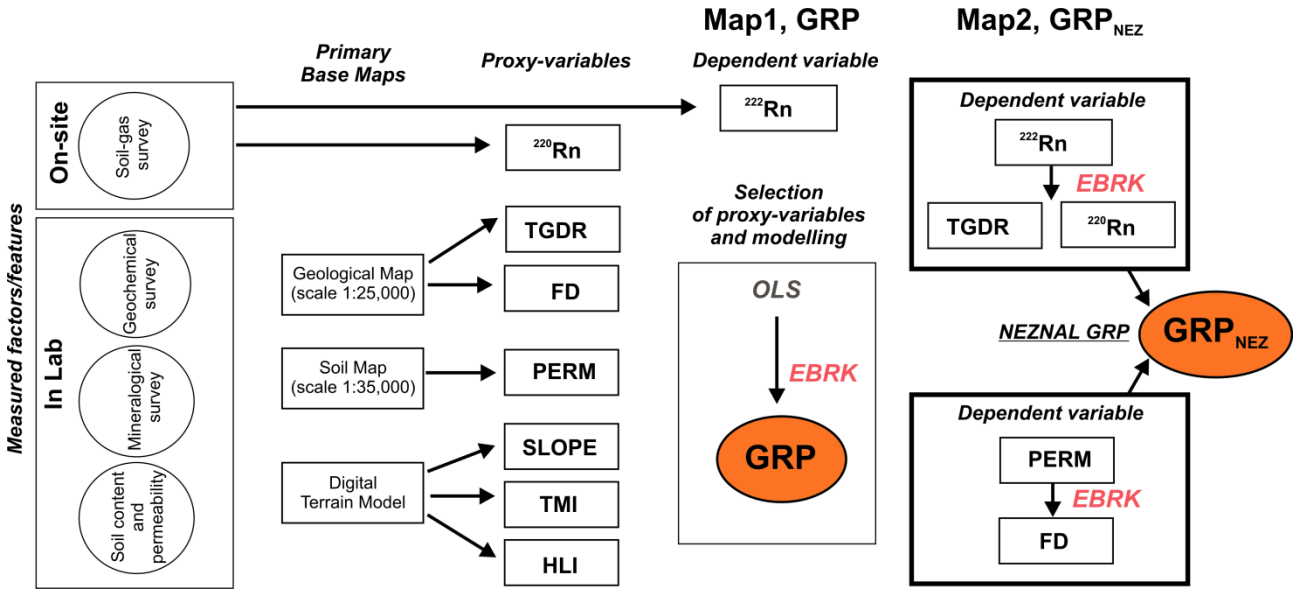

Figure 2: Flux diagram: analyses (On-site and in Lab) performed on rocks and soils and statistical data processing for the GRP maps modelling. FD = Fault density, TGDR = total gamma radiation dose, ^{220}Rn = thoron, SLOPE = digital terrain mode, TMI = moisture index, HLI = heat load index, PERM = soil permeability, OLS = Ordinary Least Square, EBRK = Empirical Bayesian Regression Kriging.

4.2 Soil-gas survey

Soil gas survey were carried out using a well-established technique that minimizes the influence of meteorological factors consisting in pounding a sampling stainless-steel probe in the soil at a depth of about 0.8 m (Ciotoli et al., 2016; Beaubien et al., 2013). Two sampling schemes were used: a random sampling (126 points) distributed in the total area (Fig. 1S), and 3 profiles (75 points) crossing a faulted zone (Table 1). Radon and thoron field measurements were carried out by using a RAD7 alpha detector (Durridge Company Inc.). This device consists in a solid-plate-ion-implanted silicon semiconductor calibrated to measure in the range between 4 and 750,000 Bq/m^3. The alpha detector is connected with the sampling probe and with a drying tube (filled with $CaSO_4$, drierite) for maintaining the relative humidity below 10%. Results were managed and corrected for relative humidity (HR) by means the specific RAD7 Data Acquisition and Analysis Software Capture® (Durridge).

Table 1: Materials and analytical methods. Schematic explanation of On-site and off-site (In Lab) measurements on samples of rock and soil.

	Type of sample	N° of samples	Analysis
On-site	Radon in soil covering the study area	126 sampling points	Soil gas (RAD7)
	Soil Radon across the main fault	75 sampling points (3 profiles)	Soil gas (RAD7)
In Lab	Rocks	130	X-Ray Fluorescence (XRF) γ-spectrometry
		4 (of 130) altered rhyolites	X-ray Diffraction Power (XRPD) Hyperspectral Analysis Raman Spectroscopy Optical Microscopy
	Colluvial soils	19 (0-20 cm depth)	X-Ray Fluorescence (XRF) γ-spectrometry Permeability (fine fraction < 63 μm)
	Alluvial soils	17 (0-20 cm depth)	γ-spectrometry Permeability (fine fraction < 63 μm)
	Alluvial soils and sediments	16 (from different soil fractions into 3 cores of 3-4 m depth)	γ-spectrometry Soil Organic Matter (%)

4.3 Mineralogical and geochemical survey

The data collection consists of 130 rock samples (updated dataset in respect to Tositti et al. 2017); 19 colluvial soil samples (from a depth of 20 cm); 17 alluvial soil samples (from a depth of 20 cm); 17 different fractions of 3 alluvial soil samples collected by surface coring (down to 3-4 m) (Table 1).

The chemical composition of rock and soil samples was determined by X-ray fluorescence (XRF) on a Philips PW2400 spectrometer, with an estimated detection limit of 0.5 wt.% for major elements, < 3% for the minor elements, and < 5% for the trace elements. ZAF method was systematically employed (Scott and Love, 1983), and the NCSDC 74301 (GSMS-1) standard (Chen and Wang, 1988) was used.

Activity concentration levels of the collected rock and soil samples were carried out by high-resolution gamma-ray spectroscopy. Samples were analysed with two p-type coaxial Hyper Pure Germanium crystal detectors by Ortec with relative efficiencies of 20% and 38%, and resolutions (FWHM) at 1332.5 keV of 1.9 keV and 1.8 keV, respectively. Both systems were calibrated for energy and efficiency using a multiple radionuclide liquid standard solution (Eckert & Ziegler Nuclitec GmbH) in a jar geometry (diameter = 56 mm; thickness = 10 mm). Spectra were acquired for 1 day to optimize peak analysis. Spectra were subsequently processed and analysed with the Gamma Vision-32 software (version 6.07, Ortec-Ametek Inc.) (Cinelli et al., 2014). ^{226}Ra was determined at 186 keV after correction for ^{235}U according to Gilmore, 2008. Conversion from bulk elemental weight fraction to the activity concentrations (Bq/kg) was obtained through the following conversion factors (Stromswold, 1995):

1% K = 309.7 Bq/kg

1 ppm U = 12.35 Bq/kg

1 ppm Th = 4.072 Bq/kg

The external dose due to natural radionuclides (Terrestrial Gamma Dose Rate, TGDR) was estimated (nGy/h) from the concentrations of natural radionuclides as follows (UNSCEAR, 2008, Cinelli et al. 2020):

$$TGDR = 0.0417 * C_K + 0.462 * C_U + 0.604 * C_{Th}$$

where C_K, C_U and C_{Th} are, respectively, the activity concentration of ^{40}K, ^{238}U and ^{232}Th in Bq/kg.

To further constrain the mineralogy and chemical composition X-ray powder diffraction (XRPD), hyperspectral analyses, and Raman spectroscopy were performed in correspondence to a set of four high-altered rocks (rhyolites).

Diffraction data were acquired on a PANalytical X'Pert PRO diffractometer operating in Bragg-Brentano reflection geometry with CoKα radiation, 40 kV voltage and 40 mA filament current, equipped with an X'Celerator detector. Qualitative analysis of diffraction data was carried out with X'Pert HighScore Plus® software (PANalytical) and the PDF-2 database.

Hyperspectral maps were done with the Headwall Photonics Micro-Hyperspec camera. This spectral camera works in the SWIR range (Short Wave InfraRed, 900-2500 nm) with a total of 166 spectral bands, 384 pixels per slit and a spatial resolution of 250 μm.

Raman measurements were made using a Thermo ScientificTM DXRTM Raman Microscope using a 532nm laser excitation source. Analyses were performed using a 50X long working distance objective with ~2.5 cm^{-1} spectral resolution, ~1 μm spatial resolution, and 25 μm pinhole operating at 3-4 mW of power. To minimize noise, each spectrum was acquired 15 times with an exposure time of 5 s. Spectra were recorded in the frequency range from 100 to 3500 cm^{-1}. Spectral fitting was carried out using the Thermo ScientificTM OMNICTM Spectra Software.

Thin sections were examined under a polarized light optical microscope (Olympus DX-50, equipped with a Nikon D7000 digital microphotography system).

4.5 Soil organic content and permeability

Soil organic matter (SOM) content of 17 different fractions of 3 alluvial soil samples collected by surface coring (down to 3-4 m) was calculated as the weight loss after combustion (Wang et al, 2013) of 5 g of alluvial soil dried.

Permeability of 19 colluvial soil samples (from a depth of 20 cm) and 15 alluvial soil samples (from a depth of 20 cm) was estimated adopting the procedure suggested by Barnet et al. (2008) from the

weight percentage of fine fraction (<63 μm). Classification (Barnet et al., 2008): < 25 wt.% = high permeability; 25 – 65 wt.% = medium permeability; > 65 25 wt.% = low permeability.

4.6 Data elaboration

4.6.1 Exploratory Data Analysis

Statistical techniques were applied to interpret collected data. In particular, Exploratory Data Analysis (EDA), which includes a range of statistical techniques, both numerical and graphical (i.e., main statistical indexes, histograms, box plots, and in some cases multivariate analyses) was applied to explore the nature of the distribution of the measured values and the presence of outliers (Ciotoli et al., 2014, and references therein).

4.6.2 Analysis and ranking of the lithologies based on their radionuclide content

In order to create ranking of the lithological types according to their average radionuclide content, the OBI index was used (Conti et al., 2019). The OBI method determines the range of overlaps of radionuclide concentrations and the overlap OBI index with respect to the upper (OBI-L) and lower (OBI-L1) bound of the overlap range (Conti et al., 2015). For this purpose, we apply the probabilistic Johnson's method (Johnson, 1949). This method allows, by the normalization of any continuous probability distribution, to define radionuclide concentration confidence intervals at 95% ranges of variability within the different lithological classes (Johnson, 1949; Miller and Miller, 2005). The application of the normalization procedure has been carried out with the SuppDists package of R (Wheeler, 2013). The OBI index with respect of the maximum (right tail of the distribution) overlap range was calculated by using the following formulas:

$OBI\_L_i = Q_{i,\,97.5} / I_{max}$ with i=1,2,….,k

OBI_L_i is generally ≥ 1 and becomes 1 when Q_i, 97.5= I_{max}

4.6.3 Ordinary Least Square regression

296 Ordinary Least Square (OLS) regression was used as the starting point for all spatial regression
297 analyses. It provides a global model of the process to understand or predict, and creates a single
298 regression equation to represent that process before to move to a local spatial model.
299 Ordinary Least Square (OLS) regression provides the soil gas radon estimate (Y) as a weighted sum
300 of the explanatory variables (Xn) with a random error term (e) (Eq. 1)
301 $y = \beta_0 + \beta_1 x_1 + \beta_2 x_2 + \ldots\ldots \beta_n x_n + \varepsilon$ (1).
302 The OLS results will provide information on:
303 - the model performance based on the values of R-squared ranging from 0 to 1;
304 - the strength and type of the relationships between each explanatory variable and the response
305 variable (i.e., Coefficients of each explanatory variable, Probability or Robust Probability and
306 Variance Inflation Factor, VIF) thus providing the selection of significant variables. For
307 example, a Variance Inflation Factor (VIF) > 7.5 indicate a high collinearity that suggests an
308 unstable model (Kleinbaum et al., 1998);
309 - the model significance;
310 - the stationarity, to determine whether the explanatory variables in the model have a consistent
311 relationship to the dependent variable both in geographic space and in data space.
312 - the model bias, assessing whether the residuals are normally distributed;
313 - the spatial autocorrelation of the residuals (by using Spatial Autocorrelation Moran's I) to
314 ensure that they are spatially random distributed in order to provide clues about missing
315 variables.
316 Further information regarding the specific meaning of the various parameters of the OLS regression
317 are reported in Ciotoli et al., 2017 and Mitchell, 2005.
318 The Empirical Bayesian Kriging Regression (EBKR) was used to combine a geostatistical
319 interpolator (e.g., kriging) with a regression analysis to make more accurate predictions than either
320 regression or kriging. In this work, EBKR was adopted to analyse the local spatial relationships
321 between the measured soil gas radon concentrations and significant proxy variables selected by the

OLS regression (see section 4.7). Furthermore, EBKR was used to combine raster maps of explanatory variables, as proxies of the radon source, migration pathways and exhalation from the soil, to make local prediction of the soil gas radon at unsampled locations.

4.6.4 Empirical Bayesian Regression Kriging

EBRK uses simple kriging (SK) to model the error term by the calculation of the semivariogram model and assuming the mean value of the dependent variable as constant. The calculation of the semivariogram is accomplished through a process of subsetting and simulations to achieve a better accuracy than other kriging methods and to allow accurate predictions of non-stationary data (Krivoruchko K. and Gribov A., 2019.; Chilès, J-P., and P. Delfiner, 1999). In order to solve the problem of multicollinearity of the explanatory variables, EBRK uses principal component analysis (PCA) to transform the explanatory variables into their principal components (PCs) and uses these principal components in the regression model. A minimum cumulative percent of variance (set to ~ 70%) for the PCs was chosen to obtain a more efficient model without loss of accuracy. Detailed description of PCA technique can be find in Cox and Donnelly (2011), and references therein, and Faraway (2006). EBRK was also applied in order to reconstruct the GRP map by using Neznal formula (GRP_{Nez}).

Descriptive statistics and graphs, and multivariate analysis were conducted using Statgraphics® Centurion XVI and Statistica 12 © Statsofts.Inc. software and R packages. Geostatistical Analyst tool included in ArcGIS Pro 2.7.0 (Copyright 2020@Esri Inc.) was using to create thematic maps.

4.7 Proxy-variables

We considered the following seven proxies (e.g., explanatory variables, Fig. 2): fault density (FD), total gamma radiation dose (TGDR), thoron (^{220}Rn), digital terrain mode (SLOPE), topography wetness index (TMI), heat load index (HLI) and soil permeability (PERM). Soil gas radon

concentration were used as dependent variable (Fig. 2). The used spatial dataset consists of 250 x 250 m raster grid of all variables (see supplementary material, Text 1S).

A more detailed description of explanatory variables follows:

i) PERM, the soil map of the Euganean Hill district (scale 1:50,000) was used to obtain the permeability of the area. The permeability affects both radon movement in the subsoil and exhalation at surface (Benavente et al., 2019; Chen et al., 2009; Neznal et al., 2005; Sun et al., 2004). Permeability categories are obtained by those reported in the soil map of the Euganean Hill (ARPAV 1995 - 2000) (Fig. 2S);

ii) FD, faults, as permeability, is considered a proxy of advective radon migration toward surface (Giustini et al., 2019; Ciotoli et al., 2017, 2007). The fault network reported in the geological map of the Euganean Hill district (scale 1:25,000) was used to construct the fault density (FD) map by kernel density estimation (KDE) (Silverman, 1986) (Fig. 3S);

iii) TGDR, the external dose due to natural radionuclides was calculated by the concentrations of natural radionuclides (^{40}K, ^{238}U, ^{232}Th) of the rock and the alluvial soil samples based on the OBI index classification and assigning the average values to the different outcropping lithologies (Fig. 4S a,b) (alluvial soil is considered equal to an outcropping lithology) (for details see Text 2S);

iv) ^{220}Rn, thoron concentration in soil gas was obtained by the on-site measurements carried out in situ with a portable RAD7 alpha detector at 126 sampling points distributed in the total area (Fig. 5S);

v) SLOPE, the digital terrain model (DMT) of the Euganean district was used to derive the slope by using the Spatial Analyst tool of ArcGIS Pro (Fig. 6Sa,b). The slope can be used as a proxy of the soil humidity, as well as of the meteorological conditions, that strongly affect the radon migration/exhalation at the soil/atmosphere boundary (Ciotoli et al., 2017);

vi) HLI and TMI indexes are also proxies of the soil moisture and temperature; these factors regulate the ^{222}Rn exhalation from the soil and thus the ^{222}Rn availability to enter buildings (Keatley et al.,

2019; Siino et al., 2019; Podstawczyńska et al., 2016; Hosoda et al., 2007). The map of the HLI (Fig. 7Sa) was derived from the digital terrain model (DMT) by using the Geomorphometry and Gradient Metrics tool in ArcGIS. The McCune and Keon (2002) method accounts for this index so that the highest values are southwest and the lowest values are northeast. A southwest slope should have warmer temperatures than a southeast slope, even though the amount of solar radiation they receive is equivalent. Additionally, this method account for steepness of slope, which is not addressed in other aspect equations. The TMI (Fig. 8S) was also estimated by the DTM (Fig. 7Sb) as a function of the slope and the upstream contributing area according to the formula TMI = ln a/ tan b, where a is the upslope contributing area (m^2) and b is the slope in radians (Boehner et al., 2006; Gessler et al., 1995).

5. Results and discussion

5.1 Soil-gas survey

As reported in the studied area description (section 3), the geology of the Euganean Hill district is characterized by the presence of volcanic (rhyolites, trachytes, latites, basalts) and sedimentary (limestones, marlstones) bedrock outcrops surrounded by an alluvial plain (Fig. 1a). For this complex geological framework, soil-gas radon measurements were considered in relation to their coincidence with the bedrock type in order to emphasize the correlation with the radon produced by the decay of its parent nuclide concentration (European Atlas, 2019; Giustini et al. 2019).

Table 2 shows main statistical parameters of the ^{222}Rn and ^{220}Rn activities measured performed in correspondence of different rocks in the Euganean Hills area. Radon measurements on the rhyolitic bedrock show the highest value (117.0 kBq/m^3) with a mean value of 31.5 kBq/m^3 and median value of 23.0 kBq/m^3 value. In contrast, the colluvial soils on sedimentary rocks display the lowest mean values of 12.0 for limestones, and 7.9 for marlstones, respectively. Thoron (^{220}Rn) concentrations follow the same trend of radon (^{222}Rn), although with very lower concentration (rhyolite shows the highest average and median values, 19.16 and 14.40 kBq/m^3 respectively). In general, all the

distributions of ^{222}Rn and ^{220}Rn activities do not appear to have a high dispersion as the standard deviation shows the same order of magnitude of the mean (Table 2).

Table 2: Descriptive statistic of soil-gas radon (^{222}Rn) and thoron (^{220}Rn) concentrations (kBq/m^3) in situ based the relative lithological bedrock.

		Radon measurements					Thoron measurements				
Bedrock	**N° samples**	**Mean**	***Median***	**St.D.**	**Min.**	**Max.**	**Mean**	***Median***	**St.D.**	**Min.**	**Max.**
Alluvial	18	48.1	29.7	59.0	0.1	243.0	16.4	10.7	16.3	0.1	47.4
Basalt	12	23.7	25.5	16.4	1.3	46.7	10.2	8.4	7.2	0.1	23.2
Latite	10	10.2	5.4	16.8	0.5	56.6	7.2	3.4	10.2	0.1	34.4
Limestone	30	12.0	4.7	16.9	0.1	57.5	6.00	3.0	9.4	0.1	35.3
Marlstone	12	7.9	2.6	13.7	0.1	47.4	4.6	3.4	4.5	0.1	11.3
Rhyolite	29	31.4	23.0	28.7	0.1	117.0	19.2	14.4	20.1	0.1	83.4
Trachyte	14	8.2	2.1	10.9	0.1	35.1	4.8	1.7	7.2	0.1	23.4

Box-plots of Figure 3 confirm that radon and thoron activities show the highest values on the rhyolitic and basaltic bedrocks, although thoron exhibits lower average concentrations. The highest values for radon and thoron (57.5 kBq/m^3 and 35.3 kBq/m^3, respectively) measured for colluvium on limestone is determined by four outliers (Fig. 3a, b). These apparently anomalous data are easily to explain considering that laccoliths generally outcrop at higher elevation, while sedimentary sequences constitute the lower flanks of the hills. In this situation, colluvium on the sedimentary sequences may contain a relevant detrital contribution from the outcropping volcanic rocks, significantly modifying radon concentration with respect to the underlying bedrock.

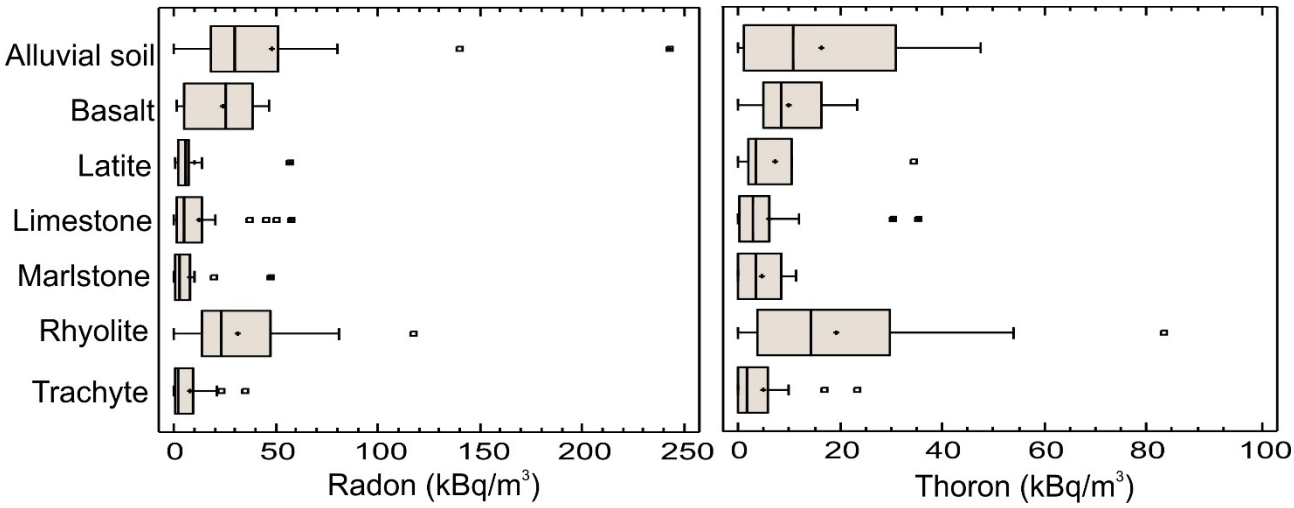

Figure 3: a) Box-and-whisker plot of radon concentration (kBq/m^3) referred to the bedrock lithology; b) Box-and-whisker plot of radon concentration (kBq/m^3) referred to the bedrock lithology.

5.1.2 Soil gas profiles across the fault system

In order to study the preferential channeling of radon migration in correspondence to structural discontinuities, three soil gas profiles (in total 75 samples) of about 1 km (P1: to the north of the study area; P2: in the middle; P3: to the south) were carried out across the main NNW-SSE fault strike, which crosses the Euganean Hills District (Fig. 4). Profiles exhibit three highest peaks with values of 147 kBq/m^3 (P1), 140 kBq/m^3 (P2), 93 kBq/m^3 (P3), respectively, east-located respect the shallow trace of the inferred fault in the geological map (Figs. 1 and 4). The highest range of values at P1 can be explained by the type of bedrock intersected by the fault system in this area. P1 profile, indeed, corresponds to the alluvial soils, the trachytic bedrock, as well as the other two profiles (P2 and P3) intersect trachyte and limestone bedrocks, and alluvial soils, characterized by a lower radionuclide concentration (Table 2, Fig. 4). In general, there are a good correlation between radon and thoron variations (Fig. 4). Anomalous higher radon peaks are concomitant, and are highlighted by the ratio ^{222}Rn/^{220}Rn, while a small amount of ^{222}Rn/^{220}Rn probably is due to bedrock microfractures. However, although the ^{222}Rn exhalation values are higher in P1 and P2 (northern and central transects), in P3 (south), the highest ^{222}Rn/^{220}Rn peak suggests the presence of a deeper source. Sequences of peaks suggest a fault architecture composed by a main fault, the constitutes the primary control on the permeability and the radon flux upward, and by a surrounding damage zone consisting of a wider interval of fractures and smaller faults which release radon concentrations of smaller magnitude.

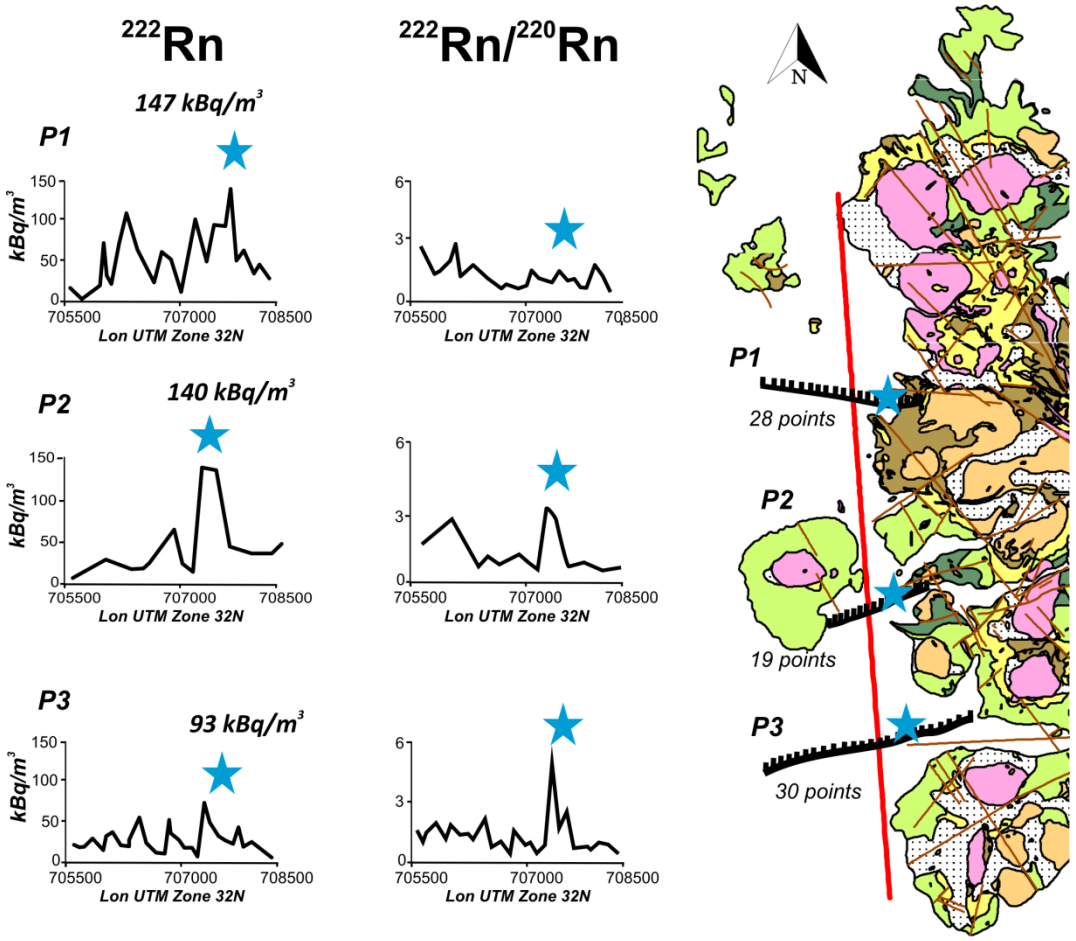

Figure 4: Influence of the presence of a fault on ^{222}Rn concentrations and ^{222}Rn /^{220}Rn in soil gas. P1, cross-section (Vò-Boccon) on the north; P2 cross-section (Brunello-Piombà) on the south; P3 cross-section (Lozzo Atestino) in the centre.

5.2 Mineralogical and geochemical survey

5.2.1 Rocks

It is well known that ^{40}K, ^{238}U and ^{232}Th radionuclide concentrations (Bq/kg) and the estimated TGDR (nGy/h) strongly depend on rock petrogenesis and geochemistry (Tositti et al., 2017; Giustini et al. 2019; European Atlas, 2019). Results from γ-spectrometry reported in Table 3 confirm the strict relationship between radionuclide content and lithology, in fact sedimentary rocks show a significantly lower radionuclide content than volcanic rocks. In particular, limestones (including the *Maiolica* and the *Scaglia Rossa* formations, Fig. 1) show the lowest values of ^{40}K, ^{238}U and ^{232}Th (88, 13 and 8 Bq/kg, respectively) which correspond to about 15 nGy/h of TGDR (Table 3). The Box-and-Whisker plot well represents the high variability of the TGDR measured in rock samples (Fig.

5a), and shows that the 29 samples of limestones are grouped at the lowest dose limit of the whole range recorded in the area. Marlstones, that are characterized by variable ratios of carbonates and clay minerals, show moderate radioactive terrestrial gamma dose (38 nGy/h), this value is slightly lower than that found in basalts (41 nGy/h, Table 2). The box-plot shows a partial overlap of the boxes (Fig. 5a). The moderate concentration of natural radionuclides in marlstone is related to their clayey fraction, as shown by the (CaO-SiO_2-Al_2O_3)-Ternary Plot representing the chemical characterization of all the collected rocks (Fig. 5b). Marlstones have higher variability, and some samples are clearly chemically distinct from the limestone group showing intermediate composition due to the presence zircons (Fig. 9S) or clays (Schön, 2015).

Consistently, volcanic formations show the highest radionuclide content which is particularly high in correspondence to rhyolites and trachytes, followed by latites and basalts (Table 3). According to the classification by Schön (2015), these data confirm the acid extrusive origin of these rocks, since ^{40}K, ^{238}U and ^{232}Th are incompatible elements partitioned into the initial melts. Thus, because of their large ionic radius and high valence of uranium and thorium isotopes, they are strongly incompatible in most rock-forming minerals and show a greatest affinity to other M^{4+} elements such as Ce and Zr. During fractional crystallization, ^{40}K is concentrated in alkali-feldspars and micas, while ^{238}U and ^{232}Th, are mainly accommodated in accessory minerals (e.g. zircon, titanite, monazite) (Bartoli et al., 2015; Damonte et al., 2017). These elements are, indeed, enriched particularly in rhyolite and trachyte formations leading to high average TGDR values (229 nGy/h and 160 nGy/h, respectively) (Tab. 3). The high standard deviation of rhyolite measurements is determined by the presence of four outliers, as shown in the box-plot (Fig. 5a).

Table 3: Descriptive statistic and concentration of natural radionuclides 40K, 238U and 232Th (Bq/kg) and the estimated Terrestrial Gamma Dose Rate estimated (TGDR, nGy/h, UNSCEAR 2008) in rock samples, and in alluvial (from quaternary plane) and colluvial topsoil samples (distinguished by the bedrock type*) randomly collected.

	type	N°samples	^{40}K	St.D.	^{238}U	St. D.	^{232}Th	St.D.	U/Th	St.D.	TGDR	St.D.
Rocks	Basalt	13	468	261	24	14	17	7	0.39	0.42	41	15
	Latite	9	1018	162	31	16	73	33	0.24	0.06	101	19

	Limestone	29	88	62	13	8	8	6	0.75	0.84	15	7
	Marlstone	8	256	131	20	15	30	22	0.53	0.56	38	14
	Rhyolite	47	1465	291	112	75	149	75	0.25	0.09	203	75
	Trachyte	24	1554	367	66	14	82	24	0.28	0.08	145	27
Soils	Alluvial	16	713	270	67	75	63	25	0.08	0.00	109	57
	Limestone*	3	157	101	14	9	15	6	0.31	0.09	76	32
	Marlstone*	1	623	302	35	6	42	23	0.24	-	69	-
	Basalt*	3	616	-	28	-	39	-	0.29	0.11	25	5
	Rhyolite*	8	736	308	52	30	59	31	0.30	0.08	101	49
	Trachyte*	4	1074	377	44	14	53	14	0.28	0.08	107	25

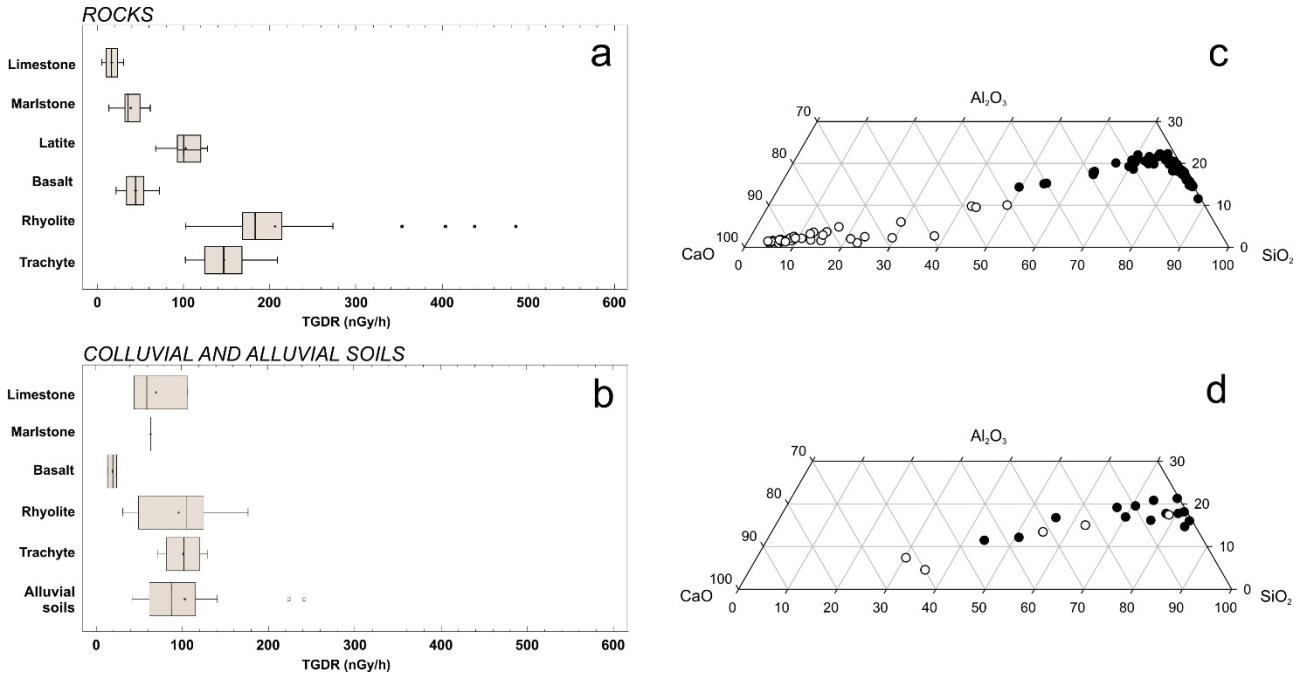

Figure 5: a) Box-and-whisker plot of TGDR measured in rock samples; b) Box-and-whisker plot of TGDR measured in colluvial and alluvial soil samples; c) Ternary plot (CaO-SiO2-Al2O3) representing the chemical characterization of rock samples (black dots = volcanic rocks; empty cycles = sedimentary rocks); d) Ternary plot (CaO-SiO2-Al2O3) representing the chemical characterization of colluvial soil samples (black dots = volcanic bedrocks; empty cycles = sedimentary bedrocks.

Macroscopically, all these four rocks (the outliers are corresponding to the samples EUR26, EUR99, FG and F) resulted to be strongly altered, showing some part with a dusty aspect. X-ray powder diffraction (XRPD) on selected altered portions of these four rocks revealed a high clay fraction enriched in ^{40}K, ^{238}U and ^{232}Th after mobilization by hydrothermal alteration (samples EUR26 and EUR99) or meteoric circulation through fault zones (sample FG and F) (Taboada et al., 2006; Dostal

et al., 2016). Diffractograms (Fig. 10S) show the high variability in secondary phases derived from alteration according to the type of environment and the stressed conditions. Alterations in samples EUR26 and EUR99 probably derived by chemical weathering as a result of hydrothermal leaching; FG and F samples were collected on a fault (strike of its surface is N-NW), in particular FG is a gouge breccia material from the core zone, F was ~2 meters far from the FG sample where the fault rock was visible less altered. EUR26 shows, beyond the presence of cristobalite, quartz, K-felspar (sanidine) and plagioclase, a higher background, in particular at low angle, that suggest the presence of clays; EUR99, has a small peak of illite/smectite mixed-layer minerals (Alboelkhair and Gaafar, 2012), probably derived by the biotite alteration. The different degree of alteration of these two last rocks was confirmed by their mineralogical characterization. The diffraction pattern of sample F (Fig. 10S) shows a low level of degradation, and the main mineralogical phases (quartz, k-felspar, plagioclase) have defined and intense peaks. On the contrary, in the diffraction pattern of sample FG (Fig. 10S) (collected on the fault breccia) the peaks of quartz and of felspars are drastically decreased, whereas an intense peak is found at low angle owing to the presence of montmorillonite-interstratified clay minerals, probably derived from the combining of chemical and mechanical weathering processes. Mixed-layers of illite-montmorillonite minerals are common alteration products in hydrothermally altered silicate rocks. These new secondary mineral phases follow the intermediate argillic alteration affects mainly plagioclase feldspars, characterized by the formation of clay minerals kaolinite and the smectite group (mainly montmorillonite) (Steiner, 1968).

Hyperspectral maps tracked very well the degree of alteration on these high-altered rhyolites (Fig. 6a). The spectrum of unaltered rhyolite in the SWIR range is basically featureless (Fig. 6b), whereas in the weathered portions the 1400 nm and 1900 nm absorption bands, indicative of OH, and the 2200 nm band, related to Al-OH bonds, are prominent and indicates the presence of clays (Fig. 6b). Spectral maps based on the 1900 nm band (the most prominent and diagnostic band) (Fig. 6a) show that the amount of altered areas on the samples surfaces is lower in the F and EUR26 samples (~40%), increases in the EUR99 sample (~50%) and reaches the maximum in the FG samples, which is

entirely affected by alteration. This pattern agrees with the secondary phases formation by alteration observed by XRPD analysis and with the ^{40}K, ^{238}U and ^{232}Th radionuclide concentrations, which is lower in F and EUR26 samples and increases in the EUR99 and FG samples respectively. A more detailed analysis with Raman spectroscopy revealed the presence of uranophane as the secondary mineral phase both in FG and F rhyolites (Fig. 6c). Uranophane crystals ($Ca(UO_2)_2(SiO_3OH)_2\ 5H_2O$) occur in their typical elongated needle-like shape (Fig. 11S) and are found along the weathered micro-fractures, typical formation related to hydrothermal alteration and fluid circulation (Fawzy and El Shaiyp, 2017). Raman analyses also showed the presence of other minor mineral phases such as pyrochlore and columbite-tantalite, containing Nb and Ta, which are also related to hydrothermal alteration (Walter et al., 2018). For a detailed Raman study of uranophane see Colmenero et al., 2019. The ratio U/Th shows that in both phenomena, hydrothermal alteration, and fault friction, do not cause a U-remobilization (Table 3). Indeed, U and Th appear both fairly increased because they are secondary phases, while are strongly increased respect K, that instead is moderately low in these samples (see Table 1S).

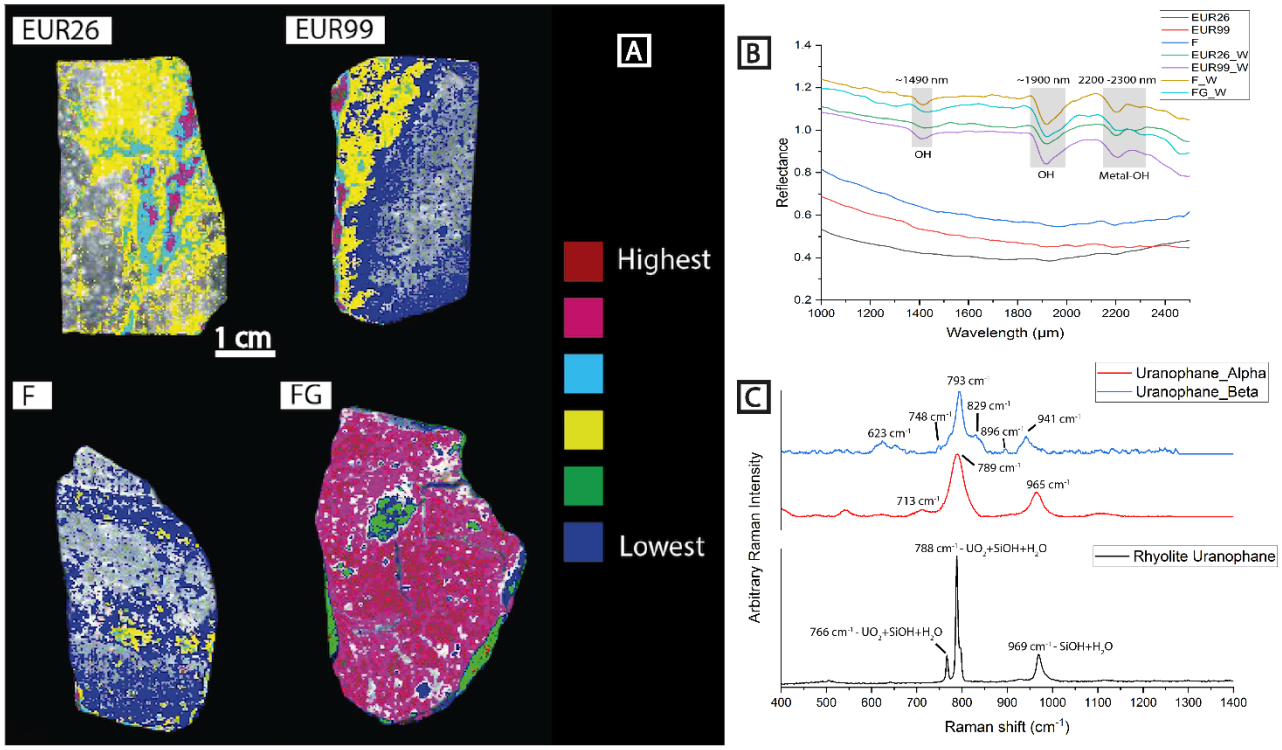

Figure 6: Mineralogical constrain of high-altered rhyolites (samples EUR26, EUR99, FG and F): a) Hyperspectral maps of the 1900 nm band. Highest values (red) correspond to deeper band depth, while lower values (blue) to shallower band depth; b) Fig. BB. SWIR spectra of the original rhyolite and the weathered portions. Original rhyolite spectra are featureless, whereas in the weathered areas the spectra show the OH absorption bands (1490 and 1900 nm) and the Metal-OH bands (between 2200 and 2300 nm). In our samples the metal-OH bonds are mainly by Al-OH in the case; c) Raman spectra of uranophane in our rhyolite samples compared to the spectra of uranophane from the RRUFF database.

5.2.2 Colluvial and alluvial soils

Natural radioactivity measured on colluvial soil samples confirms that radon exhalation is controlled by a complex interaction of different physical and geochemical factors. The ^{40}K, ^{238}U and ^{232}Th radionuclide concentrations and the estimated TGDR for colluvial soils generally agrees with those calculated for the corresponding bedrocks (e.g. colluvium on rhyolite and trachyte displays higher TGDR than colluvium on limestone), but differences are smoothed out (Table 2, Fig. 5 a, b). This observation is coherent with the differences in bulk chemistry between rocks and the corresponding colluvial soils (Figs. 5c and 5d). While the ternary variation diagram of Figure 5c shows a clear compositional separation between volcanic (balck dots) and sedimentary rocks (empty cycles) (except for some sample of marlstone characterized by high clay fraction as previously discussed), the corresponding one reported in Figure 5d shows that composition of colluvial soils displays continuous variations between to compositional extremes. This suggests that colluvial soils include different fractions of polygenic components with respect to the underlying bedrock, modifying their expected radon emanation. Natural weathering processes may lead to an increase of radioactivity due to radium enrichment on the grain surface (Sakoda et al., 2010) and alteration process causing the U-remobilization, although the U/Th ratio suggest that this phenomenon do not occur (Table 3).

Alluvial soils randomly collected in the Euganean Hill district in the alluvial plain show the highest values of U and Th (see Table 3). The average TGDR value for the alluvial topsoils (109 nGy/h) resulted to be the highest among the soil samples. Alluvial soils present the highest standard deviation, well represented in the box-whisker plots by two outliers that highly increase the average (Fig. 5b).

558

559 *5.3 Soil Organic Matter and permeability*

560 Alluvial soil cores collected in peat zones confirm a strong correlation between the soil organic matter
561 (SOM) concentration and the radioactivity values (Table 4; Fig. 7a). In general, this high TGDR in
562 alluvial soils can be attributed to high organic content that produces reduced environmental conditions
563 which favour Th- and U-concentrations (Hazen et al. 2009; Lamas, 2005; Sakoda et al., 2010). In this
564 environmental condition, U^{6+}, which is highly soluble, is reduced to insoluble U^{4+} which precipitates
565 and is adsorbed onto organic matter. Microorganisms may also play an important role in U mobility
566 inducing U precipitation in organic matter (Bone et al., 2017). On the topsoil, an additional
567 radioactive contribution might be derived from the use of phosphate fertilizers, which are often
568 enriched in U (UNSCEAR, 2008). The fraction of organic matter decreases at increasing depth, until
569 reaching sands containing residual shells and marine microorganisms (Table 4).
570 Fine fraction was also analysed on all colluvial and alluvial topsoil (20 cm) to define their
571 permeability according to Barnet et al. (2008). They show a clear difference between the two soil
572 types. Colluvial samples generally fall in a medium range of permeability, with values comprised
573 between 15 and 85% of fine fraction (< 63 μm). Alluvial soils show lower permeability than colluvial
574 soils, most of samples presenting more than 65% of fine fraction (Fig. 7b). The high content in fine
575 fraction is correlated to the presence of organic matter and abundance of clay minerals and it follows
576 the description reported in the soil permeability map (scale 1:35,000), here used as primary base map
577 for the geostatistical data processing (see Fig. 2 and the following sections).

578

579 **Table 4:** Uranium (U, ppm) concentration and Soil Organic Matter (SOM, %) of different fractions at increasing depth
580 from coring of three different alluvial soils (Vd1, Vd2 and Aq1).

	Sample (depth, cm)	^{40}K	^{238}U	^{232}Th	SOM (%)
Vd1	Vd1 (0-55)	1.44	4.60	9.3	55.05
	Vd1 (55-100)	1.12	3.70	9.9	38.32
	Vd1 (100-160)	1.18	4.30	8.1	65.03
	Vd1 (160-215)	1.07	3.60	8.1	34.24

Vd2	Vd2 (0-60)	2.23	7.80	14.7	15.36
	Vd2 (60-95)	2.75	7.30	17.4	-
	Vd2 (95-130)	1.69	4.70	8.8	9.38
	Vd2 (130-150)	1.47	4.30	6.7	7.37
	Vd2 (150-240)	1.23	3.20	6.3	5.42
	Vd2 (240-260)	0.88	3.40	3.8	5.35
Aq1	Aq1 (0-100)	2.23	3.50	1.9	4.85
	Aq1 (100-120)	2.75	2.10	4.4	5.95
	Aq1 (120-190)	1.69	4.80	2.6	3.79
	Aq1 (190-210)	0.20	3.30	2.2	1.42
	Aq1 (210-330)	-	-	-	0.59
	Aq1 (330-370)	1.27	2.50	6.4	0.57
	Aq1 (370-450)	0.90	2.30	4.5	0.37

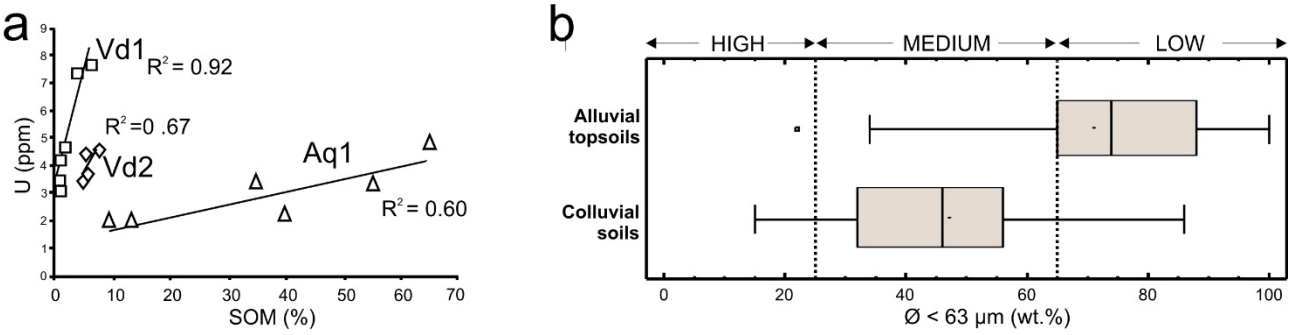

Figure 7: a) Comparison between Uranium content (ppm) and Soil Organic Matter (SOM, %) for alluvial soil fractions collected; b) Box-plot of alluvial and detritic soil permeability based on percentage of fine fraction (< 63 µm).

5.4 Modelling the Geogenic Radon Potential (GRP)

5.4.1 Preliminary selection of the proxy variables by Ordinary Least Square regression

In order to select the proxy variables to be included in the EBRK model, an Ordinary Least Square (OLS) regression model was performed to establish the correlation between the concentration of ^{222}Rn in soil gas (i.e., dependent variable) and the following 7 proxy-variables: fault density (FD), total gamma radiation dose (TGDR), thoron (^{220}Rn), digital terrain mode (SLOPE), moisture index (MI), heat load index (HLI) and soil permeability (PERM).

In the present model, none of the variables exceeds the VIF value of 7.5 indicating the absence of a redundancy among explanatory variables. Table 5 reports diagnostic parameters useful to interpret the results of the OLS model. The adjusted R^2 for the OLS model is 0.487, indicating that the OLS model explains approximately 50% of the variation in the dependent variables. Both the Joint F- and Joint Wald statistics indicates that the overall model is statistically significant; also, the Koenker statistic (0.0000, $p < 0.01$), that determine the consistency of the relationship between the dependent and the exploratory variables both in geographic space, is statically significant. This indicates that the spatial processes represented by the explanatory variables do not highlight the same behaviour everywhere in the study area (i.e., absence of stationarity). In addition, the significant Jarque-Bera statistics indicates that the residuals deviate from the normal distributed.

Table 5: Main diagnostic parameters of the OLS model.

Parameter	Value	Probability	p-value
N. Obs.	2994		
Multiple R2	0.488		
Adjusted R2	0.487		
AICc	22727		
Joint-F-statistics	476	Prob(>F), (6.2987) degrees of freedom	0.0000*
Joint-Wald-statistics	1884	Prob(>chi-squared), (6) degrees of freedom	0.0000*
Koenker-statistics	293	Prob(>chi-squared), (6) degrees of freedom	0.0000*
Jarque-Bera statistics	51	Prob(>chi-squared), (2) degrees of freedom	0.0000*
*statistical significant (p<0.01)			

Table 6: Report of the diagnostic coefficients of the OLS for each variable. Robust Probability ($p<0.05$) indicates the significance of the coefficient (i.e., the significance of the variable in the model). The most significant variables in the model includes: FD, PERM, TGDR and ^{220}Rn, where ^{220}Rn, TGDR and PERM are positively correlated, and FD is negatively correlated with the radon concentrations.

Variable	Coeff.	t-Statistics	Robust Pr	Robust_SE	VIF
Intercept	8.105	2.086	0.040*	3.948	
FD	-1.610	-5.514	0.000*	0.284	1.304
TGDR	0.005	2.189	0.017*	0.002	1.365
^{220}Rn	2.215	52.076	0.000*	0.052	1.012
TMI	-0.001	-1.175	0.265	0.000	1.001
HLI	1.950	0.623	0.580	3.528	1.010
PERM	0.471	2.016	0.040*	0.230	1.135
*statistically significant (p<0.05)					

Results suggest that soil gas radon (i.e., GRP) is strongly linked to the ^{220}Rn (Tn) distribution in soil gas and to the TGDR, naturally derived by the radioactive elements, including ^{40}K, ^{238}U, ^{232}Th and ^{226}Ra, concentrations in rocks and soils. Soil permeability (PERM) is positively correlated with radon concentration because it enhances the radon exhalation process at surface. Though HLI and TMI represent soil moisture and temperature, and thus can potentially affect soil permeability, they are not significant in the model because indirectly linked to PERM. SLOPE can promote zones of low/high soil humidity that may decrease/increase the radon concentrations at the sampling depth, however in the model the permeability is dominant respect to the topographic features.

Finally, fault density (FD) shows a significant negative coefficient. The fault density is considered representative of the fracture network (i.e., secondary permeability) which constitutes the main migration pathways for radon in the subsoil (Ioannide et al. 2013; Ciotoli et al., 2014; Drolet and Martel, 2016; Ciotoli et al. 2017). It has a very important role at territorial scale since the presence of faults can locally increase the radon hazard as highlighted by soil gas survey (see section 4.1). Probably, the local character of the faulting process explains its negative correlation in the model as opposed to permeability which constitutes a spatially more homogeneous phenomenon. On the basis of these results, only the four most significant predictors are used to construct the final GRP map: TGDR, FD, thoron, PERM.

5.4.2 Empirical Bayesian Regression Kriging (EBRK)

Empirical Bayesian Kriging Regression tool in ArcGIS Pro was applied to provide an accurate estimate of the soil gas radon concentrations (used as dependent variable) and construct the map of GRP of the Euganean Hills by using the four most significant proxy variables identified in the OLS model (Table 6). Parameters used to simulate the experimental variograms within the EBKR are reported in Figure 8 and Table 2S).

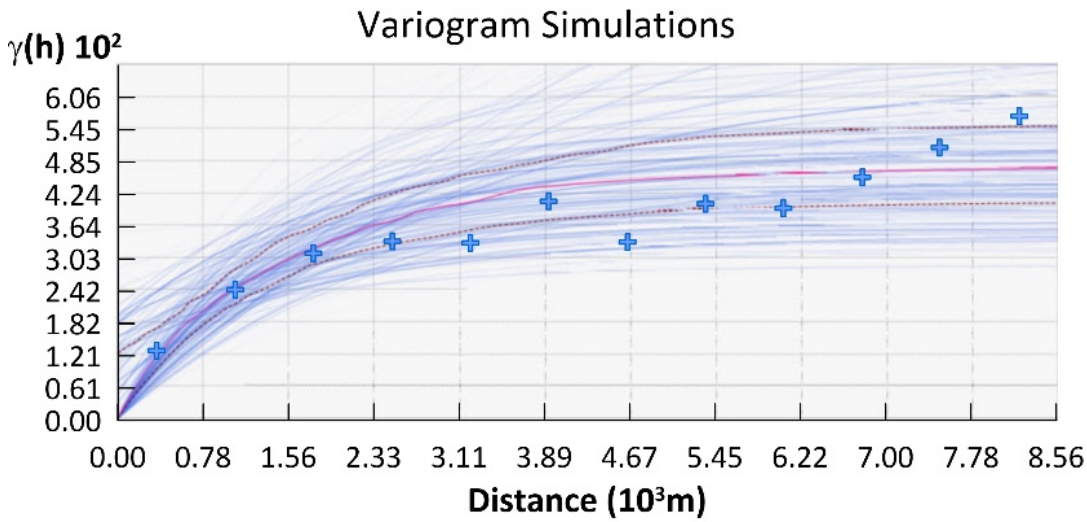

637

638 **Figure 8:** Simulated variograms and parameters used within the EBKR to construct the GRP map of the Euganean
639 Hills.

640

641 This process creates a large number of semivariograms for each subset, and the result is an empirical
642 distribution of semivariograms that are shaded by density (the darker the blue colour, the more
643 semivariograms pass through that region) (Fig. 8). The empirical semivariances are represented by
644 the blue crosses. In addition, the median of the distribution is coloured with a solid red line, and the
645 25th and 75th percentiles are coloured with red dashed lines.
646 Predictions are computed by fitting semivariograms with an exponential model and a smooth circular
647 neighbouring type with a search radius of 2000 m (see Table 2S in the supplementary).
648 The cross-validation graph shows that the predicted values of Rn concentrations (i.e., the GRP) match
649 those measured at least for low-medium values, while the higher values appear to be slightly
650 underestimated (Fig. 9a).
651 Diagnostic parameters highlight that the 4-variable model is more robust (the model of variables
652 selection is reported in Table 3S) than the 7-variable one. In particular, the model with 4 variables
653 shows (Table 7):

654 • a higher root mean squared standardized error (RMSSE) is 0.903, very close to 1 thus
655 indicating a slightly underestimation of the variability of the predictions but a better
656 performance than the 7-variable model;

- lower average standard error (ASE = 17.190) and root mean square error (RMSE = 17.424); the similarity of these two indices highlights that the model is correctly assessing the variability in prediction. Normal Probability Plot and histogram of the standardised error show a normal distribution, indicating that the model is unbiased (Fig. 9b);
- a lowest Average CRPS (8.398). CRPS measures the deviation from the predictive cumulative distribution function to each observed data value. This value should be as small as possible.

Table 7: Summary statistics of the EBRK prediction errors calculated for the models with 7 and 4 variables, respectively

Models	CRPS	RMSE	RMSSE	ASE
Model 7var: FD_TGDR_^{220}Rn _TMI_HLI_PERM_SLOPE	8.470	14.575	0.864	17.890
Model 4var: FD_TGDR_^{220}Rn _PERM	**8.398**	**17.424**	**0.903**	**17.190**

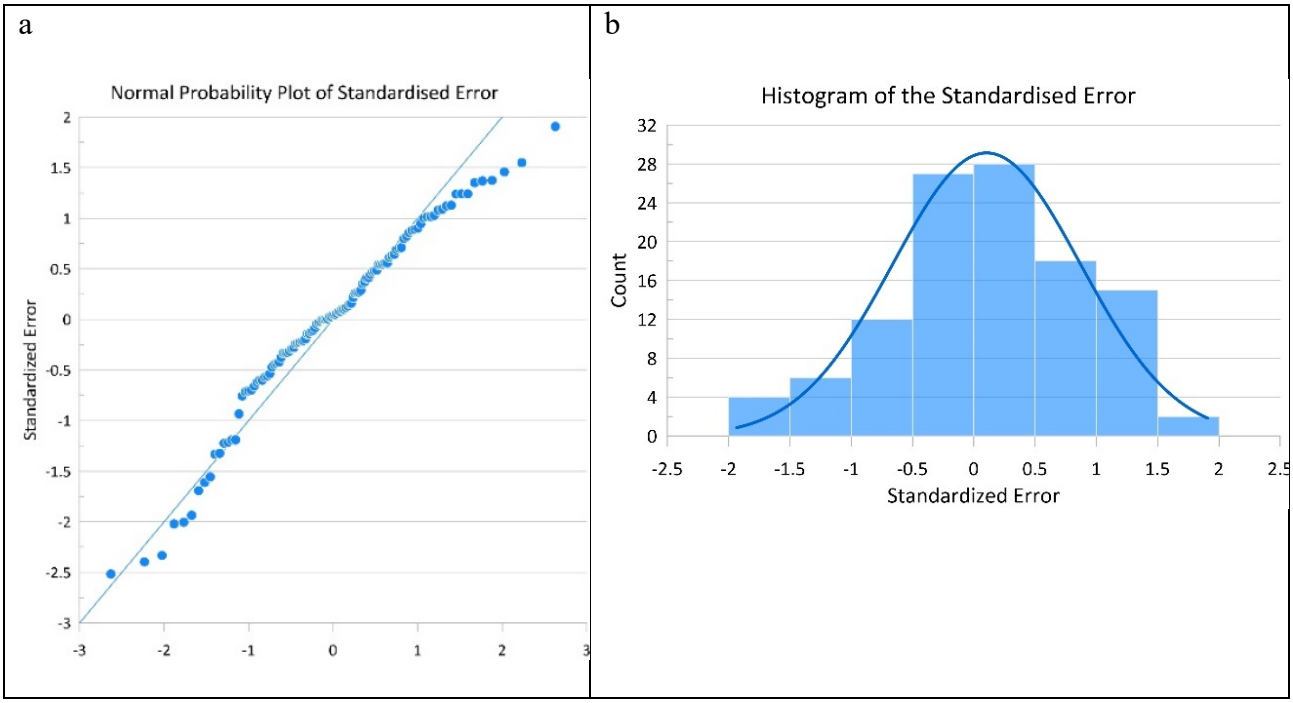

Figure 9: Diagnostic model goodness a) the normal Probability Plot; b) the histogram of the Standardised Error.

The obtained estimated GRP map in kBq/m^3 (Fig. 10) is consistent with the distribution maps of the radionuclide concentrations elaborated by Tositti et al. 2017, following the lithological distribution and outcropping, but it better represents the multivariate phenomenon also including information on

672 the influence features of the studied area (i.e., faults and permeability), in correspondence to the fault
673 system and the alluvial plain (Fig. 1).

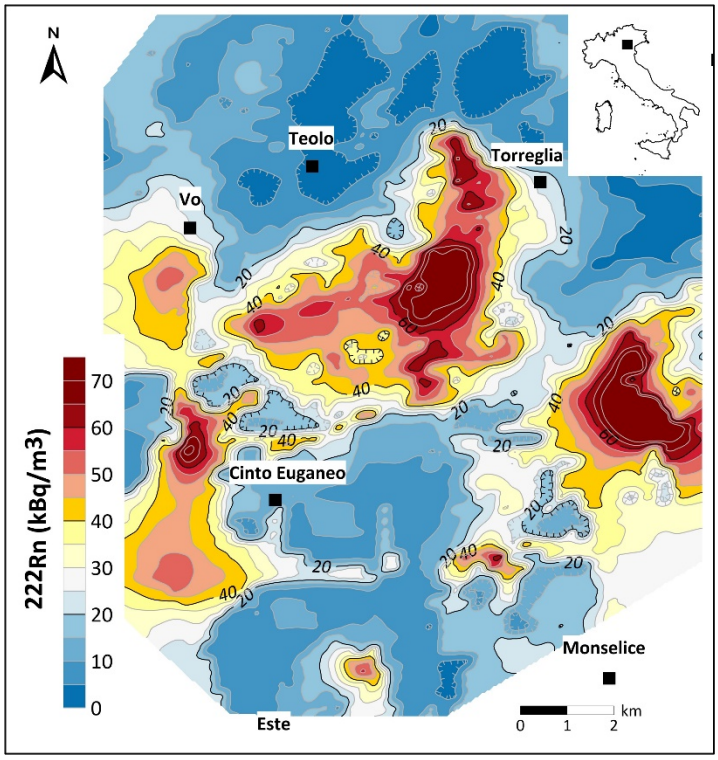

674

675 **Figure 10:** The estimated GRP map expressed in kBq/m^3

676

677 *5.4.3 Neznal Rn Potential map*

678 A second GRP map has been estimated following the Neznal approach (see formula 1, paragraph 2,
679 Neznal et al., 2004)., called hereafter $GRP_{Nez.}$ The GRP_{Nez} is dimensionless and expressed as a
680 function of the Rn concentration in soil gas (C_{Rn}) and soil gas permeability (k).
681 In this case, the EBRK was applied on the selected 4 proxies to obtain: i) the map of the estimated
682 radon by using measured Rn concentrations in soil gas as dependent variable and the maps of the
683 weighted TGDR and thoron as proxies (Fig. 11a); and ii) the map of the estimated permeability by
684 using soil permeability from the ARPAV (1995 – 2000) as dependent variable, and the fault density
685 (FD) as proxy (11 b). The standardized OBI indices were used to weight the different lithologies as a
686 function of their relative content in radionuclides (Text 2S).

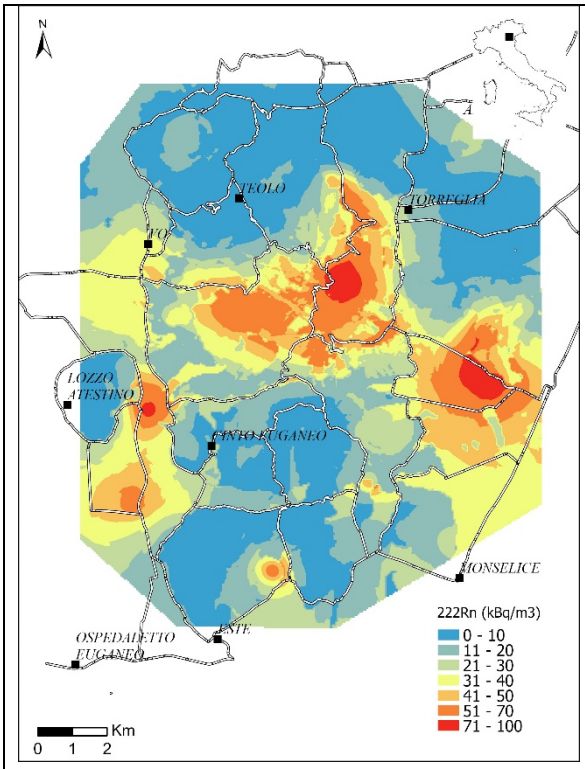

Fig. 11a: EBRK map of the estimated soil gas radon.

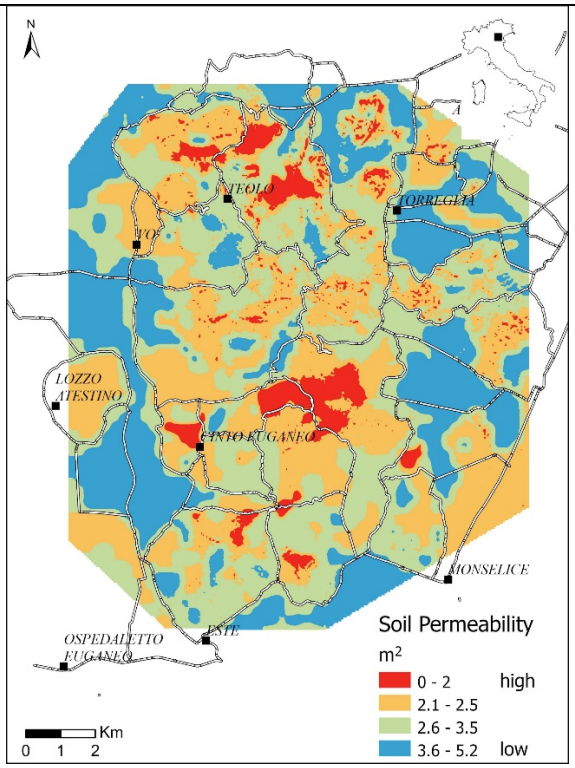

Fig. 11b: EBRK map of the estimated soil permeability.

687

688 The raster calculator tool of ArcGIS pro was used to combine the two maps (Figs. 11a and 11b)
689 according to Neznal formula. The obtained map (Figure 12) represents the GRP_{Nez} of the Euganean
690 Hills in terms of radon delivered by Earth. The standardised map show areas > 0.4 (Fig. 12)
691 corresponding to areas where are faults and the rhyolitic outcropping (see Fig. 1). The alluvial plain
692 in the south of the area returns values in the range 0.2-0.4, while the north and the south of the
693 Euganean body present the lowest values <0.2, where rhyolitic bedrocks are in small amount and
694 extension than in the central part.
695 The highest values (between 0.8 and 1) are consistently with the rhyolite outcropping in
696 correspondence to the top of the hills, where the topsoil is shallow, and the slope is rise over.
697 The high value found in the left of the map corresponds to the high radon measured along fault (Fig.
698 4).
699

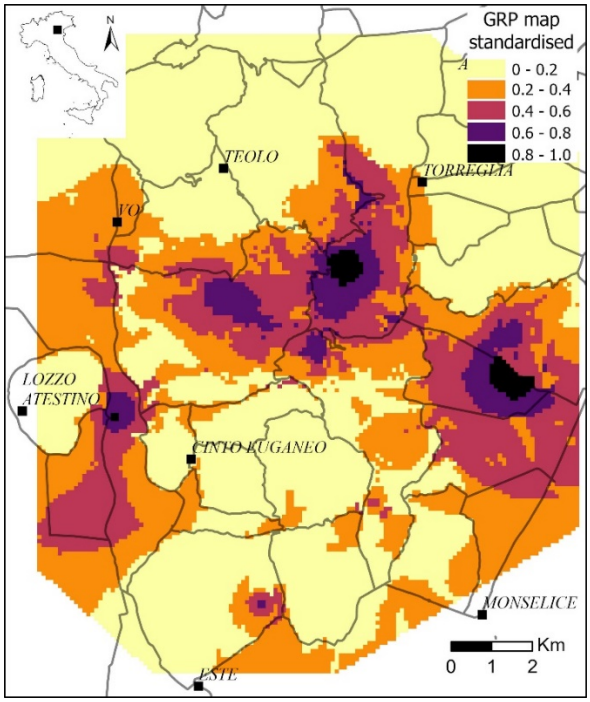

Figure 12: Standardised Geogenic Radon Potential (GRP_{Nez}) of the Euganean Hills Districts.

Quartile comparison (in terms of km^2) between the two standardized GRP maps shows very similar values (Table 8). However, the GRP_{NEZ} is a more conservative with regards to anomalous areas (above 50%).

Table 8: Summary of quartile statistics (%) in GRP and GRP_{NEZ} maps, expressed in km^2.

Quartile (%)	GRP (km^2)	GRP_{NEZ} (km^2)
<25	1.055	1.051
25-50	0.564	0.516
50-75	0.117	0.160
75-100	0.013	0.021

In order to assess the reliability of the two approaches adopted, the GRP maps were also compared (Fig. 13) operating the ratio between them. Areas were divided into three classes: i) the class 08-1.2 represents the areas in which the GRP maps coincide (ratio around 1); ii) the class with values less than 0.8, represents area where the GRP with the used EBRK on all the selected proxies (Fig. 10) prevails; and iii) the class with values greater than 1.2, represents areas where GRP_{Nez} map, that derived by the use of Neznal (Fig. 12), prevails. This comparison emphasized the good concordance

between the two approaches used, showing that approximately the 25% of the area (red area in Fig. 13) of the Euganean District falls the narrow range 08-1.2 (approximated at coincident, as equal to 1).

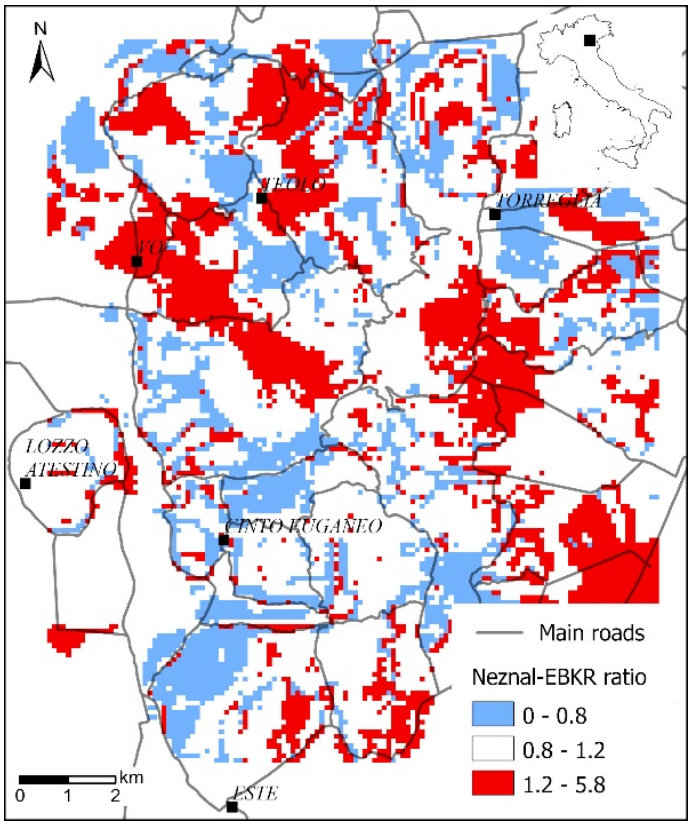

Figure 13: Comparison by the ratio between the standardised and the GRP (Fig. 10) and GRP_{Nez} (Fig. 12) maps of the Euganean Hills Districs.

6. Conclusions

Previous studies demonstrated that in the volcanic area of the Euganean Hills district (100 km^2) there were high levels of natural radioactivity. More recently, authors (Tositti et al. 2017) investigated by statistical and geostatistical analysis the correlation between local geology and radioactivity on 151 rock samples identifying high U, Th and K concentrations associated with areas characterized by trachyte and rhyolite lithologies.

The present investigation sheds further light on the relationship between local geology and radioactivity levels, extending the rocks dataset, performing on-site soil gas survey, and considering other important factors which can locally increase the radon occurrence, such as hydrothermal

731 alterations, types of soils (e.g., geochemistry or presence of organic matters), and faults. A GRP map
732 expresses in kBq/m^3 was defined using the Empirical Bayesian Regression Kriging (EBRK) to assess
733 the local spatial relationships between the measured soil gas radon concentrations and seven proxy-
734 variables: fault density (FD), total gamma radiation dose (TGDR), thoron (^{220}Rn), digital terrain mode
735 (SLOPE), moisture index (TMI), heat load index (HLI) and soil permeability (PERM). Lastly, a
736 GRP_{Nez} map was reconstructed using the Empirical Bayesian Regression Kriging (EBRK) and
737 applying the Neznal formula on a regression kriging map, expression of radon concentration, and a
738 regression kriging map, expression of soil permeability. The two maps have been compared showing
739 that are strongly coincident (in the range between 0.8 and 1.2, approximated to 1) for more than a
740 quarter of the overall area of the District.
741 More in detail, main results are the following:
742 - on site gas soil measurements random performed covering all the studied area demonstrated: i)
743 strong correlation between bedrock type and the soil radon and thoron exhalation and ii) high
744 permeability displayed along fault zones. Moreover, these results agree with XRF and γ-spectrometric
745 measurements suggesting that sedimentary bedrock may constitute a relatively thin layer above a
746 much thicker volcanic body, which can contribute to surface radon concentration. Other factors can
747 locally control the radon potential and its migration toward surface. For example, the presence of fine
748 grain sediments in the cataclastic zone related to the fault damage zone may also favors the gas
749 migration, or the presence of organic matter in the soils. In the specific case of the Euganean Hills
750 district, for its high complex geological setting, these factors can all locally compete increasing or
751 mitigating the radon occurrence.
752 - The increased rock dataset agrees with the previous results obtained (Tositti et al. 2017) and ^{40}K,
753 ^{238}U and ^{232}Th values were found particularly high in rhyolites. Descriptive statistics show four
754 outliers identified in the rhyolite group (with the highest radioactivity concentration) which were
755 deeply studied under mineralogical constrain. X-ray diffractions, hyperspectral images and Raman
756 spectroscopy confirmed this high variability in secondary phases derived from alteration according

757 to the type of environment and the stressed conditions (hydrothermal alteration and meteoric
758 circulation through fault zones).
759 - Natural radioactivity measured on colluvial and alluvial soils confirms that radon accumulation and
760 exhalation are controlled by a complex interaction of different physical and geochemical factors. In
761 particular two aspects were highlighted: i) the differences in bulk chemistry between rocks and the
762 corresponding colluvial soils due to their polygenic nature with respect to the underlying bedrock; ii)
763 the TGDR value for the alluvial top-soils resulted to be higher than any other TGDR value of colluvial
764 soil because of the high organic content that produces reduced environmental conditions favouring
765 Th- and U-concentrations. The study of alluvial soil cores (up to 3 meters of depth) collected in peat
766 zones strong correlated soil organic matter (SOM) concentration with radioactivity level measured
767 confirming a relation between these two parameters.
768 - OLS data processing permitted to define the proxy-variables useful to apply in the EBRK model
769 and to reconstruct an integrated radon concentration map. This agrees with the kriging maps obtained
770 by Tositti et al. 2017 on the radioactivity of rocks, but it is integrated with other geological and
771 topographical features that constrain the results in a more reliable way respect to the previous
772 contributions. Areas characterized by volcanic or subvolcanic lithologies and those near a favourable
773 pathway to radon migration should be of concern to promote collection of indoor radon measurements
774 and mitigation actions regardless of the determined geogenic radon potential level.
775 - The GRP_{Nez}map was obtained applying the Neznal formula by the application of regression kriging
776 between a map of the estimated soil gas radon concentration (with radon measured as dependent
777 variables and TGDR and thoron measurements as proxy-variables) and a map of the estimated
778 permeability (where the soil permeability is the dependent variable, and the fault density as proxy-
779 variables). The highest of the five classes obtained reflected the contribution due to the radon sources
780 (derived in particular by volcanic bedrock types and alluvial soil) and the permeability factor
781 especially identified with the fault presence.

- Both the approaches here implemented for estimating the GRP of the studied area turned out to be useful mapping tools. They can be tested in future in other geological contexts. In case a good coincidence the GRP using all the proxy directly by the EBRK can be a promising alternative to the Neznal approach in terms of time consuming.

Practically, the obtained results provide a powerful scientific background for planning new effective radon-prevention strategies in the studied area and support future indoor survey. They can actually be a meaningful support to local administrations for an up-to-date land use planning, according to the threshold levels stipulated by the Council Directive 2013/59/Euratom.

The Euganean Hills District (Italy) resulted to be a very significant case of study for increasing knowledge in geogenic radon assessment and in mapping its related hazard for several aspects: the state of the art furnished by the previous works, the dwelling density, the high radioactivity levels measured in the past, as well as its complex local geology and topography.

Acknowledgments

This study was funded by Project CPDA134483 of the University of Padova (RS).

Captions

Figures:

Figure 1: a) Sketch map of the investigated area; b) Scheme of a rhyolite dome on a sedimentary stratigraphy.

Figure 2: Flux diagram: analyses (On-site and in Lab) performed on rocks and soils and statistical data processing for the GRP maps modelling.

Figure 3: a) Box-and-whisker plot of radon concentration (kBq/m^3) referred to the bedrock lithology; b) Box-and-whisker plot of radon concentration (kBq/m^3) referred to the bedrock lithology.

806 Figure 4: Influence of the presence of a fault on ^{222}Rn concentrations and $^{222}Rn/^{220}Rn$ in soil gas. P1,
807 cross-section (Vò-Boccon) on the north; P2 cross-section (Brunello-Piombà) on the south; P3 cross-
808 section (Lozzo Atestino) in the centre.
809 Figure 5: a) Box-and-whisker plot of TGDR measured in rock samples; b) Box-and-whisker plot of
810 TGDR measured in colluvial soil samples; c) Ternary plot (CaO-SiO2-Al2O3) representing the
811 chemical characterization of rock samples; d) Ternary plot (CaO-SiO2-Al2O3) representing the
812 chemical characterization of colluvial soil samples.
813 Fig. 6: Mineralogical constrain of high-altered rhyolites (samples EUR26, EUR99, FG and F): a)
814 Hyperspectral maps of the 1900 nm band. Highest values (red) correspond to deeper band depth,
815 while lower values (blue) to shallower band depth; b) Fig. BB. SWIR spectra of the original rhyolite
816 and the weathered portions. Original rhyolite spectra are featureless, whereas in the weathered areas
817 the spectra show the OH absorption bands (1490 and 1900 nm) and the Metal-OH bands (between
818 2200 and 2300 nm). In our samples the metal-OH bonds are mainly by Al-OH in the case; c) Raman
819 spectra of uranophane in our rhyolite samples compared to the spectra of uranophane from the
820 RRUFF database. For a detailed Raman study of uranophane see Colmenero et al., 2019.
821 Figure 7: a) Comparison between Uranium content (ppm) and Soil Organic Matter (SOM, %) for
822 alluvial soil fractions collected; b) Box-plot of alluvial and detritic soil permeability based on
823 percentage of fine fraction (< 63 μm).
824 Figure 8: Simulated variograms and parameters used within the EBKR to construct the GRP map of
825 the Euganean Hills.
826 Figure 9: Diagnostic model goodness a) the normal Probability Plot; b) the histogram of the
827 Standardised Error.
828 Figure 10: The estimated GRP concentration expressed in kBq/m^3.
829 Figure 11: a) EBRK map of the estimated soil gas radon; b) EBRK map of the estimated soil
830 permeability.
831 Figure 12: Geogenic Radon Hazard Index of the Euganean Hills District.

832 Figure 13: Comparison by the ratio between the standardised and the GRP (Fig. 10) and GRPNez
833 (Fig. 12) maps of the Euganean Hills Districs.
834
835 **Tables:**
836 Table 1: Materials and analytical methods. Schematic explanation of On-site and off-site (In Lab)
837 measurements on samples of rock and soil.
838 Table 2: Descriptive statistic of soil-gas radon (kBq/m3) concentrations in situ based the relative
839 lithological bedrock.
840 Table 3: Descriptive statistic and concentration of natural radionuclides 40K, 238U and 232Th
841 (Bq/kg) and the estimated Terrestrial Gamma Dose Rate estimated (TGDR, nGy/h, UNSCEAR 2008)
842 in rock samples, and in alluvial (from quaternary plane) and colluvial topsoil samples (distinguished
843 by the bedrock type*) randomly collected.
844 Table 4: Uranium (U, ppm) concentration and Soil Organic Matter (SOM, %) of different fractions
845 at increasing depth from coring of three different alluvial soils (Vd1, Vd2 and Aq1).
846 Table 5: Main diagnostic parameters of the OLS model.
847 Table 6: OLS diagnostic coefficients for each variable.
848 Table 7: Summary statistics of the EBRK prediction errors calculated for the models with 7 and 4
849 variables, respectively
850 Table 8: Summary of quartile statistics (%) in GRP and GRP_{NEZ} maps, expressed in sq km.
851
852 **Supplementary materials:**
853 **Tables:**
854 Table 1S: The EBRK process: input data is divided into overlapping 3 subsets of 50 points per
855 subset. In each subset, semivariograms are estimated in each of the performed simulations (100
856 simulations).

857 Table 2S: Natural radionuclide concentration ^{232}Th (ppm), ^{238}U (ppm) and ^{40}K (%), and the U/Th

858 ratio in all rock samples.

859 Table 3S: Diagnostic parameters of EBRK models calculated used a combination of proxy variables

860 gradually eliminating the proxies from the highest to the lowest robust p-value of table 5.

861

862 **Figures:**

863 Figure 1S: Soil gas survey samples (red cycles) and rock and soil collected samples (white sqaure).

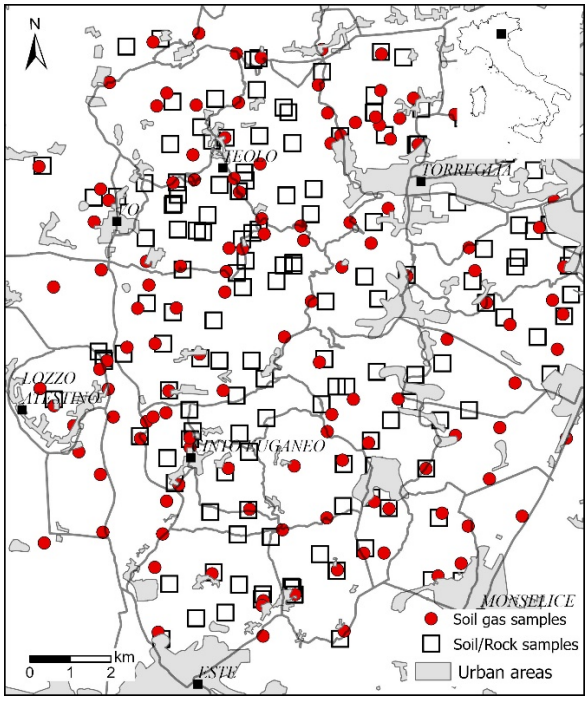

864

865

866 Figure 2S: PERM map of the Euganean Hill district (scale 1:50,000) (from ARPAV 1995 - 2000).

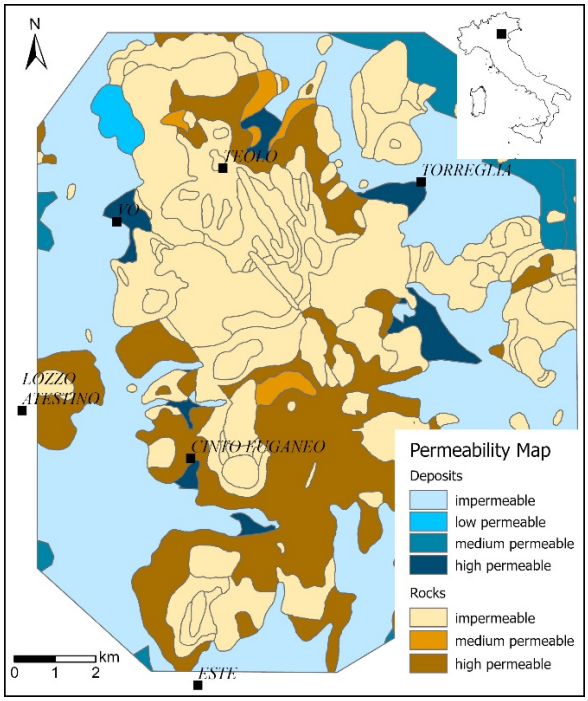

867

868

869

870 Figure 3S: FD, fault density map by kernel density estimation (KDE) (from the geological map of the

871 Euganean Hill district (scale 1:25,000).

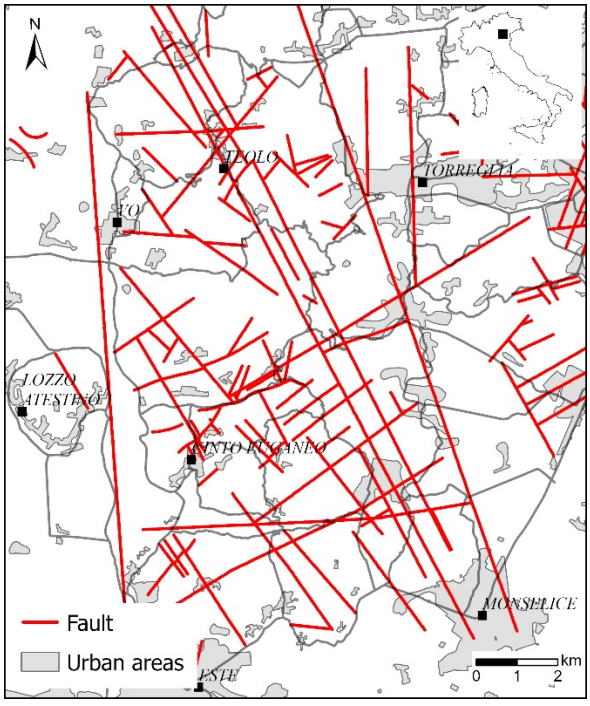

872

873

Figure 4S: a) simplified map of outcropping lithologies (alluvial soil is considered equal to an outcropping lithology) of the Euganean Hill district; b) TGDR, terrestrial gamma dose rate map calculated by the ^{40}K, ^{238}U, ^{232}Th concentrations of the rock and the alluvial soil samples (Fig. 1S).

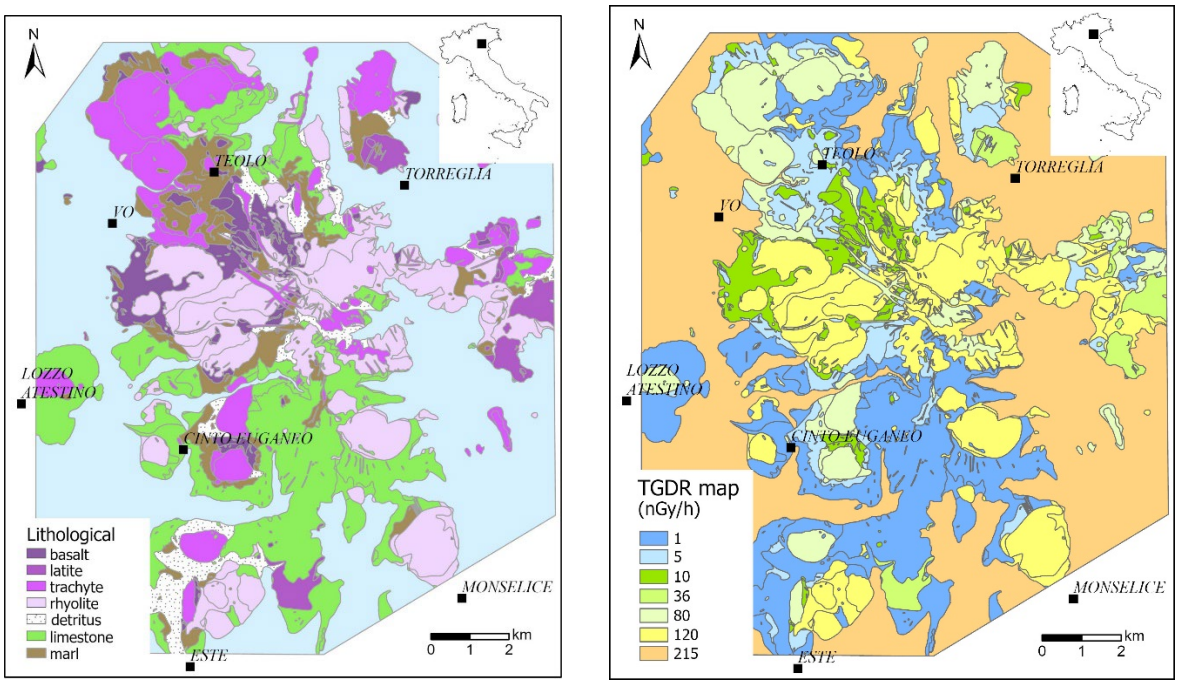

Figure 5S: ^{220}Rn, thoron concentration map obtained by the on-site measurements carried out in situ with a portable RAD7 alpha detector at 126 sampling points distributed in the total area (Fig. 1S).

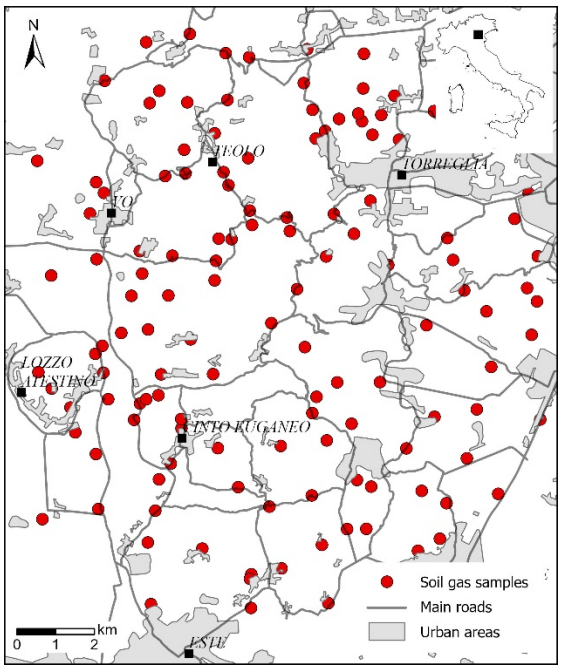

Figure 6S: a) The digital terrain model (DMT), and b) the SLOPE map derived.

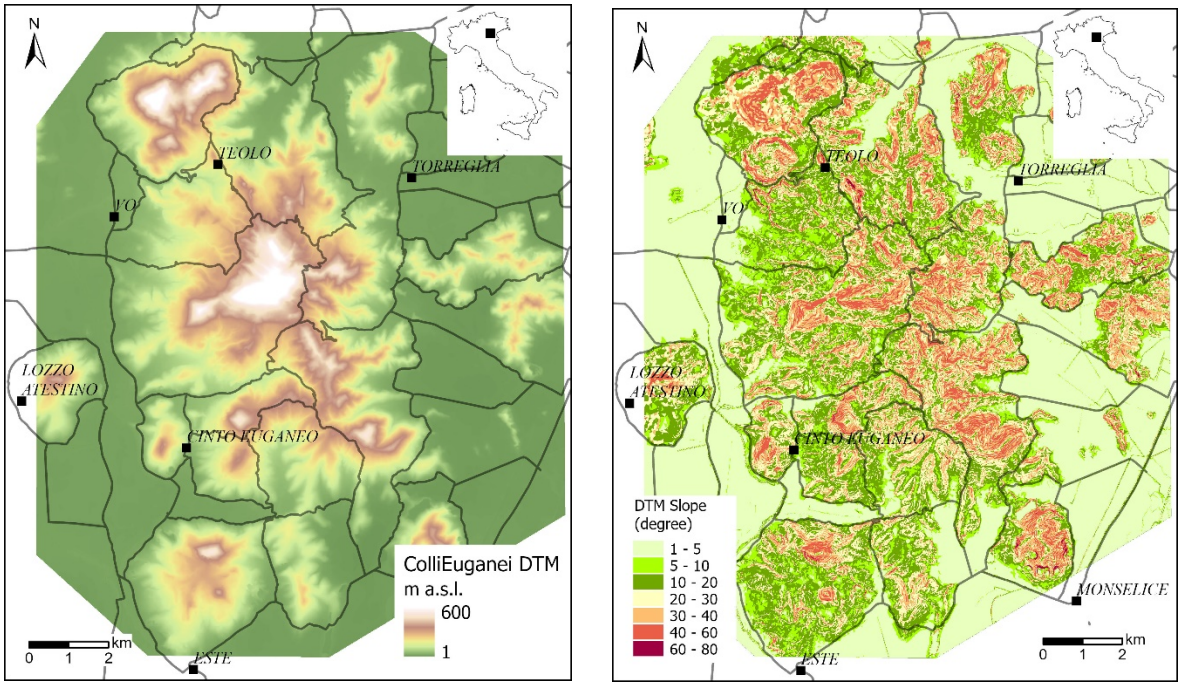

883

884 Figure 7S: a) HLI, the Heat Load Index map derived from the digital terrain model (DMT) (Fig.

885 6Sa).

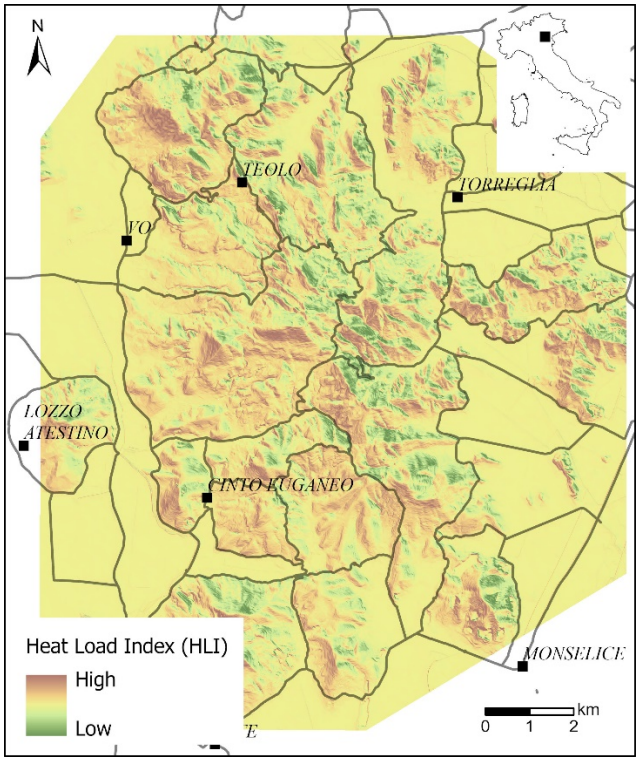

886

887 Figure 8S: TMI, Topographic Moisture Index map derived from the digital terrain model (DMT) (Fig.

888 6Sa).

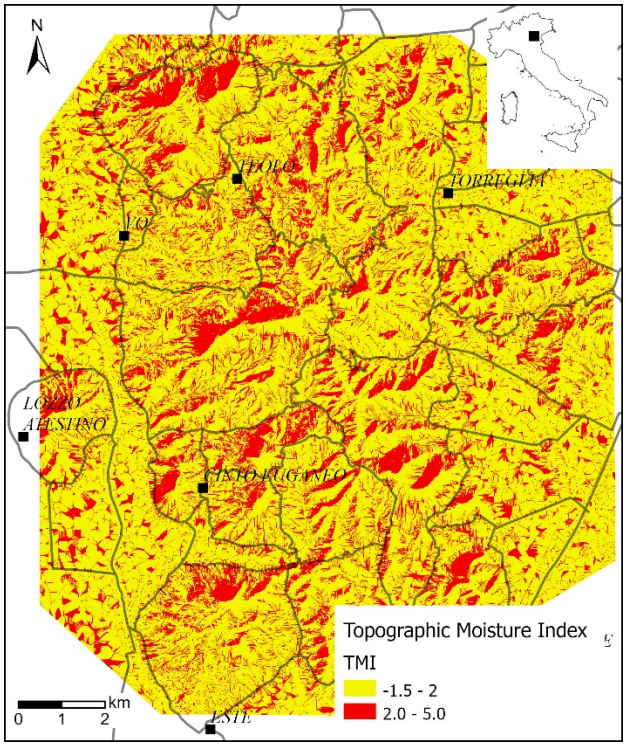

889

890 Figure 9S: a) Backscattered Electron Scanning Electron Microscopy (BSE-SEM) image of a
891 marlstone containing zircon. Sample from Faedo (Euganean Hills).

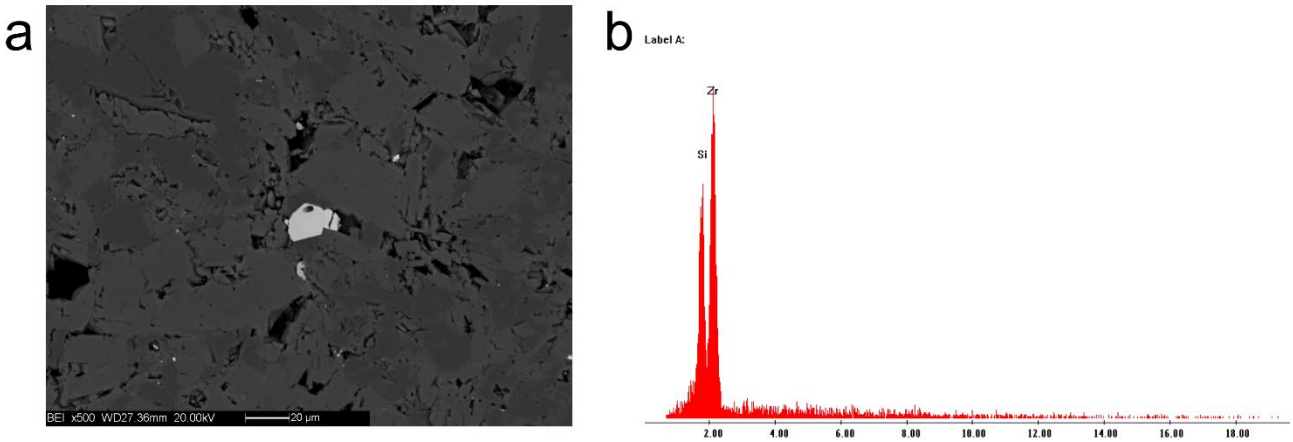

892

893 Figure 10S: Comparison between the diffraction patterns (samples EUR26, EUR99, FG and F).
894 Mineral abbreviations after Whitney and Evans (2010): Qz = quartz; Sa = sanidine; Pl = plagioclase;
895 Crs = cristobalite; Ilt/sme = illite/smectite; Mnt = montmorillonite.

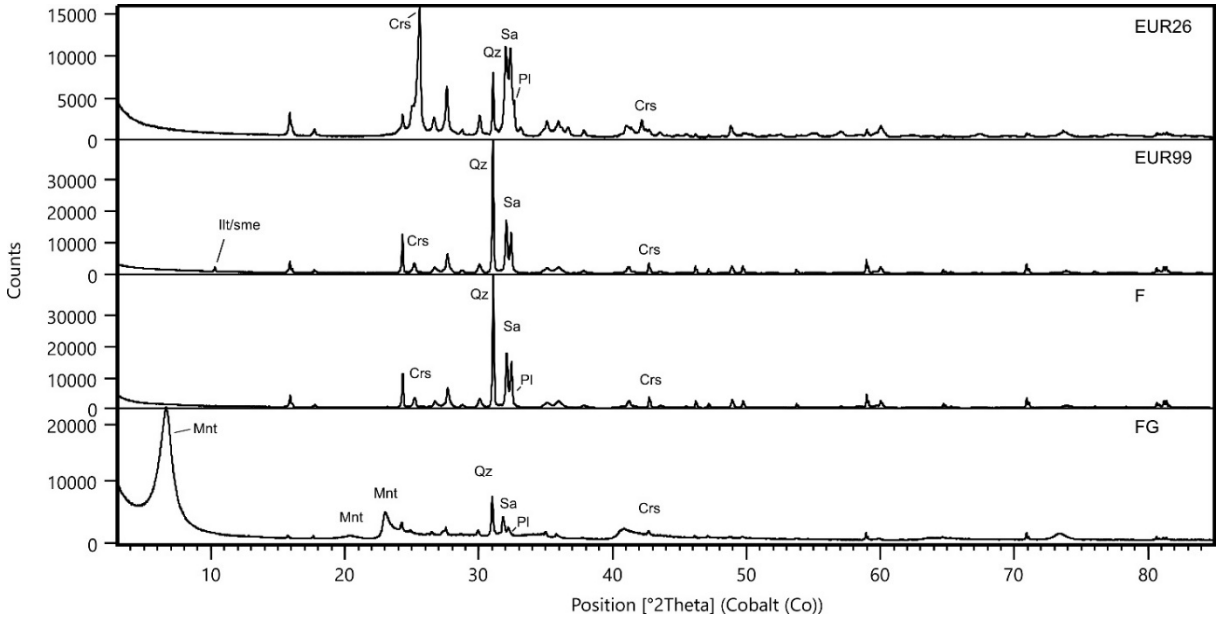

Figure 11S: Microscope images (reflected light) of elongated uranophane (Urn) crystals found in an alteration vein (sample FG).

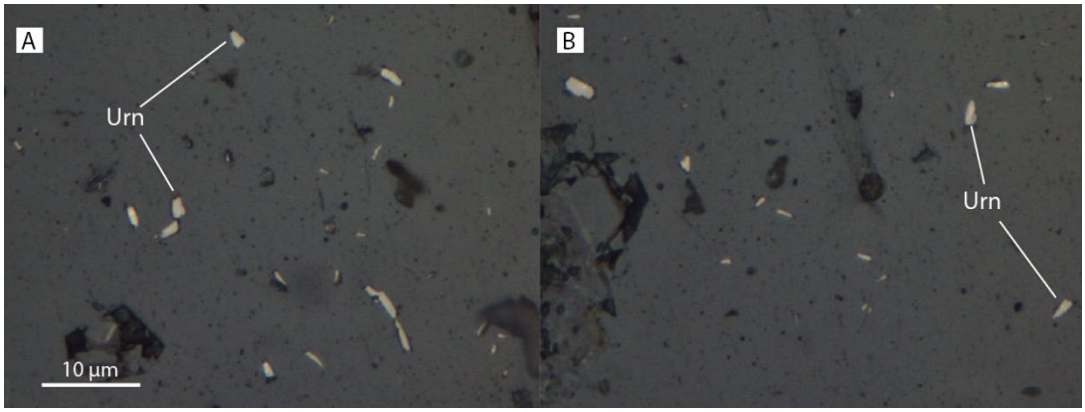

Text:

Text 1S: Principal Component Analysis (PCA) description.

Text 2S: OBI standardization for each lithological class and the related TGDR weighted map.

Text 3S: A) EBRK statistics for the estimation of source model (radon); B) EBRK statistics for the estimation of migration model (permeability).

References

1. ANPA (2000). Il sistema informativo territoriale per la valutazione del potenziale di esalazione di radon dal suolo, 1–63.
2. ARPAV - Servizio Osservatorio Suolo e Bonifiche, Carta dei suoli della provincia di Padova, 1995 – 2000, https://www.arpa.veneto.it/.
3. Appleton J.D. (2006) Radon in air and water. In: Selinus O. et al. (Eds) Medical Geology, Elsevier, 227–262.
4. Barnet I., Pacherová P., Neznal M. (2008). Radon in geological environment - Czech experience, Geological Survey Special Papers, No. 19.
5. Bartoli O, Meli S., Bergomi M.A., Sassi R., Magaraci D., Liu D-Y. (2015) Geochemistry and zircon U-Pb geochronology of magmatic enclaves in trachytes from the Euganean Hills (NE Italy): further constraints on Oligocene magmatism in the eastern Southern Alps, European Journal of Mineralogy, 27, 161–174.
6. Bertolo A. and Bigliotto C., (2009). Il radon nei Colli Euganei (Veneto): aspetti metodologici e ambientali per l'individuazione delle zone a rischio su piccola scala. Controllo ambientale degli agenti fisici: nuove prospettive e problematiche emergenti - Vercelli, 24-27 marzo 2009. Available on 29 July 2021 at: https://www.arpa.piemonte.it/arpa-comunica/events/eventi-2009/atti-convegno-agenti-fisici/bertolo1.pdf
7. Bochicchio, F. et al. Results of the Representative Italian National Survey on Radon Indoors. Health Phys. 17(5), 741-748 (1996)

8. Bone S. E., Dynes J. J., Cliff J., Bargar J.R. (2017). Uranium(IV) adsorption by natural organic matter in anoxic sediments. Proceedings of the National Academy of Sciences of the United States of America, 114(4), 711–716.
9. Chen, G., Wang, J., 1998. The preparation of marine geological certified reference materials - polymetallic nodule GSPN-1 and marine sediment GSMS-1 from the Central Pacific Ocean, Geostandards and Geoanalytical Research 22, 119–125.
10. Chilès, J-P., and P. Delfiner (1999). Chapter 4 of Geostatistics: Modeling Spatial Uncertainty. New York: John Wiley & Sons, Inc.
11. Cinelli G., Tositti L., Capaccioni B., Brattich E., Mostacci D. (2014). Soil gas radon assessment and development of a radon risk map in Bolena, Central Italy, Environmental Geochemistry and Health 37, 305–319.
12. Cinelli G., Brattich E., Coletti C., de Ingeniis V., Mazzoli C., Mostacci D., Sassi R., Tositti L., Terrestrial gamma dose rate mapping (Euganean Hills, Italy): comparison between field measurements and HPGe gamma spectrometric data, Radiation Effects and Defects in Solids 175(1-2):54-67
13. Ciotoli G., Sciarra A., Ruggiero L., Annunziatellis A., Bigi S. (2016). Soil gas geochemical behaviour across buried and exposed faults during the 24 August 2016 central Italy earthquake. Annals of Geophysics, 59, Fast Track 5.
14. Ciotoli G., Voltaggio M., Tuccimei P., Soligo M., Pasculli A., Beaubien S.E., Bigi S. (2017) Geographically weighted regression and geostatistical techniques to construct the geogenic radon potential map of the Lazio region: A methodological proposal for the European Atlas of Natural Radiation, Journal of Environmental Radioactivity, 166, 355–375
15. Colmenero F., Plášil J. & Sejkora J. (2019). The layered uranyl silicate mineral uranophane-β: crystal structure, mechanical properties, Raman spectrum and comparison with the α-polymorph. Dalton Transactions, 48(44), 16722-16736.
16. Council Directive 2013/59/Euratom 5/12/2013

17. Conti M.E., Tudino M.B., Finoia M.G., Simone C., J. (2019) Performance of two Patagonian molluscs as trace metal biomonitors: The overlap bioaccumulation index (OBI) as an integrative tool for the management of marine ecosystems, Ecological Indicators, 101, 749-758, doi.org/10.1016/j.ecolind.2019.01.060)
18. Cox D. R. and Donnelly Christl A., (2011) Principles of Applied Statistics, 10.1017/CBO9781139005036
19. Cuney M. 2014, Felsic magmatism and uranium deposits, Bulletin de la Societe Geologique de France, t. 185, no 2, pp. 75–92.
20. Damonte L.C., Rivas P.C., Pasquevich A.F., Andreola F., Bondioli F., Ferrari A.M., Tositti L., Cinelli G., 2017. Structural Characterization of Natural and Processed Zircons with X-Rays and Nuclear Techniques, Advances in Condensed Matter Physics, vol. 2017, Article ID 9707604, 9 pages. https://doi.org/10.1155/2017/9707604
21. Dgr n.79 del 18/01/2002, Attuazione della raccomandazione europea n. 143/90: interventi di prevenzione dall' inquinamento da gas radon in ambienti di vita.
22. Dostal J., van Hengstum T.R., Shellnutt J.G., Hanley J.J. (2016). Petrogenetic evolution of Late Paleozoic rhyolites of the Harvey Group, southwestern New Brunswick (Canada) hosting uranium mineralization. Contrib. Mineral. Petrol. 171:59. https://doi.org/10.1007/s00410-016-1270–8.
23. Drolet J.F. and Martel R., Distance to faults as a proxy for radon gas concentration in dwellings, Journal of Environmental Radioactivity 152 (2016) 8–15.
24. European Commission, Joint Research Centre – Cinelli G, De Cort M & Tollefsen T (Eds.), European Atlas of Natural Radiation, Publication Office of the European Union, Luxembourg, 2019; Printed version: ISBN 978-92-76-08259-0; doi:10.2760/520053 ; Catalogue number KJ-02-19-425-EN-C; Online version: ISBN 978-92-76-08258-3; doi:10.2760/46388 ; Catalogue number KJ-02-19-425-EN-N; https://remon.jrc.ec.europa.eu/About/Atlas-of-Natural-Radiation/Download-page

25. European Commission, 2021, Communication - COM(2021)44, Europe's Beating Cancer Plan, https://ec.europa.eu/health/sites/default/files/non_communicable_diseases/docs/eu_cancer-plan_en.pdf
26. Faraway, Julian J. (2006). Extending the Linear Model With R: Generalized Linear, Mixed Effects and Nonparametric Regression Models. Boca Raton, FL: Chapman & Hall/CRC, 301 pp
27. Fawzy K. M. & El Shayip J. B. (2017). Mineralogy and radioactivity of anomalous sites of Wadi Murrah post-collision granites, south Eastern Desert, Egypt. Arabian Journal of Geosciences, 10(7), 160.
28. Hazen R.M., Ewing R.C., Sverjensky D.A. (2009) Evolution of uranium and thorium minerals. American Mineralogist 94, 1293–1311.
29. IARC (1998) Man-made Mineral Fibres and Radon, IARC monograph on the evaluation of cancinogenic risck to humans, Volume 43, Lyon, France
30. ISPRA, Istituto Superiore per la Protezione e la Ricerca Ambientale. (2012). Note illustrative della Carta geologica dei Colli Euganei alla scala 1:50000. Padova Sud. Foglio 147.
31. Ioannide K., Papachristodoulou C., Stamoulis K., Karamanis D., Pavlides S., Chatzipetros A., Karakala E., Soil gas radon: a tool for exploring active fault zones, Applied Radiation and Isotopes 59 (2003) 205–213.
32. Johnson, N. L. *(1949). "Systems of Frequency Curves Generated by Methods of Translation"*. Biometrika. *36 (1/2): 149–176.* doi:10.2307/2332539. JSTOR 2332539.
33. R. Gilmore Practical Gamma-ray Spectrometry – 2nd Edition Gordon 2008 John Wiley & Sons, Ltd. ISBN: 978-0-470-86196-7
34. Kleinbaum D.G., Kupper L.L., Muller K.E., Nizam A., 1998. Applied Regression Analysis and Other Multivariable Methods, Duxbury Press, Belmont, CA.
35. Krivoruchko K. and Gribov A., 2019, Evaluation of empirical Bayesian kriging," Spatial Statistics Volume 32. https://doi.org/10.1016/j.spasta.2019.100368

1005 36. Kropat G., Bochud F., Murith C., Palachos Gruson M., Baechler S. (2017). Modeling of geogenic
1006 radon in Switzerland based on ordered logic regression, Journal of Environmental Radioactivity
1007 166, 376–381.
1008 37. Lamas M.C. (2005). Factors affecting the availability of uranium in soils. Landbauforschung
1009 Völkenrode Sonderheft 278. Braunschweig Federal Agricultural Research Centre (FAL).
1010 38. Miller J.N., Miller J.C., Statistics and chemometrics for analytical chemistry, fifth eds. Pearson,
1011 Prentice Hall, Essex, UK.
1012 39. Mitchell, Andy.The ESRI Guide to GIS Analysis, Volume 2. ESRI Press, 2005.
1013 40. Massironi M., Zampieri D., Caporali A., Miocene to Present major fault linkages through the
1014 Adriatic indenter and the Austroalpine-Penninic collisional wedge (Alps of NE Italy). In:
1015 MORATTI, G. & CHALOUAN, A. (eds) Tectonics of the Western Mediterranean Region and
1016 North Africa. Geological Society, London, Special Publication 262, 245–258, 2006.
1017 41. MetroRADON: Metrology for radon monitoring 2017-2020. Documents can be downloaded
1018 from the web page, http://metroradon.eu/
1019 42. J.N. Miller, J.C. Miller Statistics and Chemometrics for Analytical Chemistry (fifth ed.), Pearson,
1020 Prentice Hall, Essex, UK (2005)
1021 43. National Research Council (US) (1999). Committee on Health Risks of Exposure to Radon
1022 (BEIR VI). Health Effects of Exposure to Radon: BEIR VI. Washington (DC): National
1023 Academies Press (US). Available from: https://www.ncbi.nlm.nih.gov/books/NBK233262/ doi:
1024 10.17226/5499
1025 44. Nazaroff W.W., Moed B.A., Sextro R.G. (1988). Soil as a source of indoor radon: generation,
1026 migration and entry. In Nazaroff W.W., Nero A.V. (eds). Radon and its decay products in indoor
1027 air. Wiley and Sons, 57–112.
1028 45. Neznal M., Neznal M., Matolín M., Barnet I.,Miksova J. (2004). The new method for assessing
1029 the radon risk of building sites. Czech Geological Survey Special Papers 16, Czech Geological
1030 Survey, Prague, 47 pp. http://www.radonvos.cz/pdf/metodika.pdf

1031 46. Piccoli, G., Sedea, R., Bellati, R., Di Lallo, E., Medizza, F., Girardi, A., De Pieri, R., De Vecchi,
1032 G.P., Gregnagnin, A., Piccirillo, E.M., Norinelli, A., Dal Pra' A. (1981). Note illustrative della
1033 Carta geologica dei Colli Euganei alla scala 1:25000. II Edizione. Memorie di Scienze
1034 Geologiche 34, 523-566.
1035 47. Plant J.A., Reeder S., Salminen R., Smith D.B., Tarvainen T., De Vivo B., Peterson M.G. (2003).
1036 The distribution of uranium over Europe: geological and environmental significance. Appl Earth
1037 Sci 256(3):473–480.
1038 48. Pola M., Ricciato A., Fantoni R., Fabbri P., Zampieri D. (2014). Architecture of the western
1039 margin of the North Adriatic foreland: the Schio-Vicenza fault system. Italian Journal of
1040 Geosciences 133, 223–234.
1041 49. Pola M., Fabbri P., Piccinini L., Zampieri D. (2015). Conceptual and numerical models of a
1042 tectonically-controlled geothermal system: a case study of the Euganean Geothermal System,
1043 Northern Italy. Central European Geology 58, 129–151.
1044 50. Popit A., Vaupotic J., (2002). Indoor radon concentrations in relation to geology in Slovenia.
1045 Environmental Geology 42, 330–337.
1046 51. Sakoda A., Nishiyama Y., Hanamoto K., Ishimori Y., Yamamoto Y., Kataoka T., Kawabe A.,
1047 Yamaoka K. (2010) Differences of natural radioactivity and radon emanation fraction among
1048 constituent minerals of rock or soil, Applied Radiation and Isotopes 68, 1180–1184
1049 52. Scott V.D., Love G., 1983. Quantitative Electron Probe Microanalysis. John Wiley and Sons,
1050 New York.
1051 53. Schoen J.H. Physical Properties of Rocks - Fundamentals and Principles of Petrophysics, 2015
1052 2nd Ed. Elsevier ISBN: 978-0-100404-3
1053 54. Silverman, B. W. Density Estimation for Statistics and Data Analysis. New York: Chapman and
1054 Hall, 1986.
1055 55. Steiner A., Clay minerals in hydrothermally altered rock at Wairakei, New Zeland, Clays and
1056 Clay Minerals, 1968, Vol. 16, pp. 193-213.

56. Strati V., Baldoncini M., Bezzon G.P, Broggini C., Buso G.P., Caciolli A., Callegari I., Carmignani L, Colonna T, Fiorentini G., Guastaldi E., Kaçeli Xhixhaf M., Mantovani F, Menegazzo R., Moub L., Rossi Alvarez C., Xhixha G., Zanon A., 2014. Total natural radioactivity, Veneto (Italy). Journal of Maps, Vol. 11, Issue 4, 545–551.http://doi.org/10.1080/17445647.2014.923348.

57. Stromswold D.C., 1995. Calibration facilities for borehole and surface environmental radiation measurements, Journal of Radioanalytical and Nuclear Chemistry 194, 393–401

58. Sundal A.V., Henriksen H., Lauritzen S. E., Soldal O., Strand T., Valen V. (2004) Geological and geochemical factors affecting radon concentrations in dwellings located on permeable glacial sediments - a case study from Kinsarvik, Norway. Environmental Geology, 45, 843–858.

59. Taboada T., Martínez Cortizas A., García C., García-Rodeja E. (2006). Uranium and thorium in weathering and pedogenetic profiles developed on granitic rocks from NW Spain. Sci. Total Environ. 356, 192–206.

60. Tositti L., Cinelli G., Brattich E., Galgaro A., Mostacci D., Mazzoli C., Massironi M., Sassi R. (2017). Assessment of lithogenic radioactivity in the Euganean Hills magmatic district (NE Italy), Journal of Environmental Radioactivity 166, 1–11.

61. Trotti, F., Biancotto, R., Lanciai, M., Mozzo, P., Predicatori, F., Tacconi, A., 1994. Indoor exposure to natural radioactivity in Veneto. Radiat. Prot. Dosim. 56 (1-4), 309-313.

62. Trotti, F., Tanferi, A., Lanciai, M., Mozzo, P., Panepinto, V., Poli, S., Predicatori, F., Righetti, F., Tacconi, A., Zorzine, R., 1998. Mapping of areas with elevated indoor radon levels in Veneto. Radiat. Prot. Dosim. 78 (1), 11-14.

63. Trotti, F., Tanferi, A., Bissolo, F., Fustegato, R., Lanciai, M., Mozzo, P., Predicatori, F., Querini, P., Righetti, F., Tacconi, A., 1999. A Survey to Map Areas with Elevated Indoor Radon Levels in Veneto, Radon in the Living Environment, 19-23 April 1999, Athens, Greece, pp. 859-868.

64. UNSCEAR (2008). Sources and Effects of Ionizing Radiation, I Annex, BISBN 978-92-1-142274-0.

65. UNSCEAR (2010). United Nations Scientific Committee on the Effects of Atomic Radiation Report: "Summary of low-dose radiation effects on health".
66. Viganò A., Scafidi D., Ranalli G., Martin S., Della Vedova B., Spallarossa D., (2015). Earthquake relocations, crustal rheology, and active deformation in the central–eastern Alps (N Italy), Tectonophysics 661, 81–98
67. Viganò A., Zampieri D., Rossato S., Martin S., Selli L., Prosser G., Ivy-Ochs S., Campedel P., Fedrizzi F., Franceschi M., Rigo M. (2018). Past to present deformation of the central-eastern Southern Alps: from the foreland to the Giudicarie belt, Periodico semestrale del Servizio Geologico d'Italia - ISPRA e della Società Geologica Italiana Geol. F. Trips Maps, Vol.10 No.1.1, 1–78.
68. Walter B. F., Parsapoor A., Braunger S., Marks M. A. W., Wenzel T., Martin M. & Markl G. (2018). Pyrochlore as a monitor for magmatic and hydrothermal processes in carbonatites from the Kaiserstuhl volcanic complex (SW Germany). Chemical Geology, 498, 1-16.
69. Wang J., Wang X., Zhang J., 2013. Evaluating Loss-on-Ignition Method for Determinations of Soil Organic and Inorganic Carbon in Arid Soils of Northwestern China, Pedosphere, Vol. 23, Issue 5, 593–599.
70. Wheeler, B., 2013. SuppDists: supplementary distributions. R package version 1: 1–9.1.
71. WHO, 2009. In: Zeeb, H., Shannoun, F. (Eds.), Handbook on indoor radon – a public health perspective. ISBN 978 92 4 154767, available at: http://apps.who.int/iris/ bitstream/10665/44149/1/9789241547673_eng.pdf. [accessed 19.11.15.].
72. Wichmann H.E., Schaffrath Rosarioa A., Heida I.M., Kreuzerc M., Heinricha J., Kreienbrockd L. (2005) Lung cancer risk due to radon in dwellings-evaluation of the epidemiological knowledge, International Congress Series 1276, 54–57.
73. Yarmoshenko I., Vasilyev A., Malinovsky G., Bossew P., Žunić Z.S., Onischenko A., Zhukovskya M. (2016) Variance of indoor radon concentration: Major influencing factors, Science of The Total Environment, Volume 541, 155–160.

74. Benavente D., Valdés-Abellán J., Pla C., Sanz-Rubio E., Estimation of soil gas permeability for assessing radon risk using Rosetta pedotransfer function based on soil texture and water content. J Environ Radioact. 2019 Nov;208-209:105992. doi: 10.1016/j.jenvrad.2019.105992. Epub 2019 Jun 18. PMID: 31226584.
75. Neznal Matej, Neznal Martin, 2005. Permeability as an important parameter for radon risk classification of foundation soils. Annals of Geophysics, 48(1), 175-180.
76. Sunil Dhar, Surjeet Singh Randhawa, Arvind Kumar, Vivek Walia, Ching-Chou Fu, Harish Bharti, Arun Kumar. (2021) Decomposition of continuous soil–gas radon time series data observed at Dharamshala region of NW Himalayas, India for seismic studies. Journal of Radioanalytical and Nuclear Chemistry 327:2, pages 1019-1035.
77. Masahiro HOSODA, Michikuni SHIMO, Masato SUGINO, Masahide FURUKAWA & Masahiro FUKUSHI (2007) Effect of Soil Moisture Content on Radon and Thoron Exhalation, Journal of Nuclear Science and Technology, 44:4, 664-672, DOI: 10.1080/18811248.2007.9711855
78. Keatley, Nicholas L., Soil moisture influences on radon fluxes in the Sydney Basin, BEnviSci Hons, School of Earth, Atmospheric & Life Sciences, University of Wollongong, 2019. https://ro.uow.edu.au/thsci/174
79. Podstawczyńska, Agnieszka and Pawlak, Włodzimierz. "Soil heat flux and air temperature as factors of radon (Rn-222) concentration in the near-ground air layer" Nukleonika, vol.61, no.3, 2016, pp.231-237. https://doi.org/10.1515/nuka-2016-0039
80. McCune, Bruce and Dylan Keon, 2002. Equations for potential annual direct incident radiation and heat load index. Journal of Vegetation Science. 13:603-606.
81. Gessler, P.E., I.D. Moore, N.J. McKenzie, and P.J. Ryan. (1995). Soil-landscape modeling and spatial prediction of soil attributes. International Journal of GIS. 9(4):421-432.

82. Boehner, J., Selige, T. (2006): Spatial Prediction of Soil Attributes Using Terrain Analysis and Climate Regionalisation' In: Boehner, J., McCloy, K.R., Strobl, J.: 'SAGA - Analysis and Modelling Applications', Goettinger Geographische Abhandlungen, Vol.115, p.13-27

83. D.L. Whitney, B.W. Evans, Abbreviations for names of rock-forming minerals, Am. Mineral. 95 (2010) 185–187.

Websites:

http://www.handbookofmineralogy.org/pdfs/uranophane-alpha.pdf

https://www.unscear.org/docs/publications/2017/UNSCEAR_2017_Report.pdf

https://www.unscear.org/docs/publications/2000/UNSCEAR_2000_Annex-B.pdf